DIATOM ALCHEMY

A Thesis
Presented to
The Academic Faculty

By

Christopher Stephen Gaddis

In Partial Fulfillment
Of the Requirements for the Degree
Master of Science in Materials Science and Engineering

Georgia Institute of Technology
August 2004

Diatom Alchemy

Approved By:

Dr. Ken Sandhage

Dr. Bob Snyder

Dr. Meilin Liu

August 15. 2004

Dedication

To the memory of Valentino DeGiusti

ACKNOWLEDGEMENT

Thank you to my advisor Dr. Sandhage for encouraging me, and for all the useful discussions we had in developing this work. Thank you to my parents for introducing me to the curiosities of the world early in life, and for nurturing my creativity. Thank you to the Omniplex science museum for exposing me to all the cool and fascinating exhibits, which got me excited about learning science in my early years. Finally, thanks to all my bros and girlfriends for keeping me sane and happy during all this.

TABLE OF CONTENTS

LIST OF FIGURES

SUMMARY

This work resulted in the development of multiple distinct and novel methods of cheaply producing large numbers of biologically derived, complex, 3-dimensional microstructures in a multitude of possible compositions. The biologically derived structures employed in this work were diatoms, a type of single celled algae, which grow complex silica shells in species-specific shapes. Due to the wide diversity of naturally occurring diatom shapes (on the order of 10^5), and the flexibility in tailoring chemical compositions using the methods developed here, real potential exists for cheaply mass-producing industrially relevant quantities of controlled shape and size 3-d particles for the first time. The central theme of this research is the use of diatoms as a transient scaffold onto which a coating is applied. After curing the coating, and in some cases firing the coating to form ceramic, the diatom can be selectively etched away leaving a free standing replica of the original structure with the salient features of the pre-form intact, but now composed of a completely different material. Using this concept, specific methods were developed to suit various precursors. Dip coating techniques were used to create epoxy diatoms, and silicon carbide diatoms. The Sol-Gel method was used to synthesize zirconia diatoms in both the tetragonal and monoclinic phases. A multi step method was developed in which previously synthesized epoxy diatoms were used as a template for deposition of a silicon carbide precursor and then heat treated to produce a silicon carbide/carbon multi-component ceramic. A hydrothermal reaction was also developed to convert Titania diatoms to barium titanate by reaction with barium hydroxide. Finally, the device potential of diatom-derived structures was conclusively demonstrated by constructing a gas sensor from a single Titania diatom. Under suitable

conditions, the sensor was found to have the fastest response and recovery time of any sensor of this type reported in the literature. Furthermore, this work has laid the groundwork for the synthesis of many other tailored compositions of diatoms, and provided several compositions for device creation.

CHAPTER 1

INTRODUCTION

Significant global effort is underway to develop shape-tailored microstructures with fine (down to nanoscale) features for medical, cosmetic, aerospace, environmental, agricultural, optical, fluidic, and microelectromechanical applications[1-12]. Interest in controlled shape assemblages of nanoparticles have exhibited, or have been predicted to exhibit, unique and attractive properties relative to structures comprised of more macroscopic particles[1-4]. As a result, appreciable global activity is underway to identify methods for synthesizing nanoparticles and nanoparticle-based structures with well-controlled chemistries, precise shapes, and fine features[5]. Microfabrication routes based on layer-by-layer (2-D) techniques, such as lithographic micromachining methods developed for the silicon microelectronics industry, are not particularly well suited for fabricating 3-D structures with complex shapes (e.g., curved 3-D surfaces) and with very fine (down to nanoscale) features[6,7]. However, alternative approaches capable of direct 3-D micro/nanofabrication must also to be scalable to allow for high-throughput production[7]. Processing approaches that can be scaled up for high-throughput production on a massive (up to tonnage) scale, while retaining structural and chemical precision on a fine (down to nanometer) scale, are needed in order for the widespread technological promise of such nanoparticle-based structures to be realized. These often-conflicting requirements may be addressed by fabrication paradigms that rely upon the simultaneous assembly of large numbers of identical 3-D nanoparticle structures on a fine scale and continuous production on a large scale may be satisfied through the use of self-assembly

processes[8,9]. Nature is particularly adept at massively parallel nanoscale self-assembly. Numerous examples can be found in nature of microorganisms that, through sustained reproduction (i.e., repeated doubling), can assemble enormous numbers of similar bioclastic structures with microscale 3-D shapes and meso-to-nano-scale features[10-12]. Natural microorganisms direct the assembly of mineralized (bioclastic) nanoparticle-based structures with complex, but reproducible 3-D shapes[15-20]. Among the best known and most striking examples are diatoms (Bacillariophyta), which generate a particularly impressive range of shaped structures.[15-17].

Diatoms are single-celled algae that populate a diverse range of aquatic environments (marine and freshwater), which range over virtually every body of water on earth[18-20]. Each diatom cell forms a rigid wall (frustule) consisting of a 3-D microscopic assemblage of amorphous silica nanoparticles[10-12]. Each diatom species forms a uniquely-shaped frustule with fine features (10^2 nm pores, ridges, protuberances, etc.) arrayed in intricate, species-specific patterns[11,12]. Such morphological specificity is a strong indication that the frustule assembly process is under genetic control[23]. The maximum dimensions of such frustules can range from <1 micron to $>10^2$ microns, whereas the fine, regular features distributed on the frustule wall possess characteristic dimensions of 10^1-10^2 nanometers[18-20]. A wide diversity in frustule shapes and features can be found among the tens of thousands of diatom species that are known to exist, as is illustrated in the secondary electron images in Figure 1-1[19,24]. Under appropriate growth conditions, diatom reproduction can occur several times per day, so that enormous numbers of similarly-shaped frustules can be generated in a relatively short period of

time (e.g. at a sustained reproduction rate of 2 per day, more than 1 billion frustules of similar shape would be generated in 15 days, and more than 1 billion billion, would be produced in 1 month). Sustained reproduction (repeated doubling) of a given diatom species can yield enormous numbers of descendant diatoms with similarly-shaped frustules (e.g., 40 sustained reproduction cycles would yield 2^{40} or more than 1 trillion frustules of similar geometry).[25] Such massively-parallel and precise self-assembly of 3-D nanoparticle structures under ambient conditions is a highly-attractive characteristic for nanotechnological applications. Large scale commercial culturing of diatoms has already been demonstrated[14]. Diatoms have been used as a food source for commercial fish production. Furthermore, the estimated 10^5 extant diatom species provide a considerable selection of frustule shapes and fine features for potential devices. In particular, the very high surface area to volume ratios found in diatoms is attractive for many device applications. However, the widespread use of natural diatom frustules in device applications is limited by the properties of amorphous silica. Attempts to incorporate other oxides, such as germania, into diatoms during reproduction have yielded meager changes in frustule composition to date (e.g., the isotopic Ge/Si ratio taken up in the cell walls of Nitzschia alba upon reproduction was reported to be only up to 0.02 wt%). An alternate approach would be to separate the biological replication and chemical modification processes into independent, sequential steps (i.e., to alter the frustule composition after diatom reproduction is completed). This approach, referred to as the BaSIC (Bioclastic and Shape-preserving Inorganic Conversion) process, has recently been demonstrated by converting diatom frustules into frustule-shaped magnesium oxide via reaction with magnesium gas at 900°C. However, the range of compositions that may

be accessed via such gas/silica displacement reactions is limited to reactants with: i) higher affinities for oxygen than silica, and ii) relatively high vapor pressures at modest temperatures (so as to be able to conduct the reaction at temperatures below which appreciable coarsening, and loss of fine frustule features, would occur). Other shape-preserving chemical modification processes are needed to expand the range of accessible compositions and properties. This work demonstrates several new methods of altering diatom chemistry, while preserving frustule shape and fine features.

The primary drawback to using gas/silica displacement reactions to convert diatom chemistry is that the set of possible reactions is limited to those that are thermodynamically favorable. The products of the reaction must be more stable than the reactants. Since silica is a fairly stable material, the number of possible reactions is significantly restricted. An alternative approach that the author developed is to neglect diatom chemistry and simply utilize the feature of interest, diatom geometry. By applying a thin continuous coating of a non-silica material to diatom frustules, such that the interior and exterior surfaces are coated, the coating takes on the shape of the diatom, which effectively results in diatoms of a new chemical composition. For some potential applications such as catalysis, gas sensing, or fluorescence, the new surface chemistry of the thin coating applied to the frustule may impart the desired functionality. In other cases it may be desirable to remove the diatom silica underlying the applied coating. This can be accomplished using a selective etch. Several silica etching chemicals have been identified, including hydrofluoric acid, sodium hydroxide, and sodium fluoride. To selectively remove silica without dissolving the coating, an etchant must be chosen which either does not react with the coating, or reacts much slower with the coating than silica.

A further consideration that must be made is the phase of the silica dissolution products. If the dissolution products are gaseous, as in the case of hydrofluoric acid, which produces hydrogen and silicon tetrafluoride upon reaction with silica, the rate of the reaction must be slow enough that the evolved gasses can escape without destroying the coating. The coatings used thus far have been sufficiently porous that gasses can escape if the dissolution is conducted at a reasonable rate.

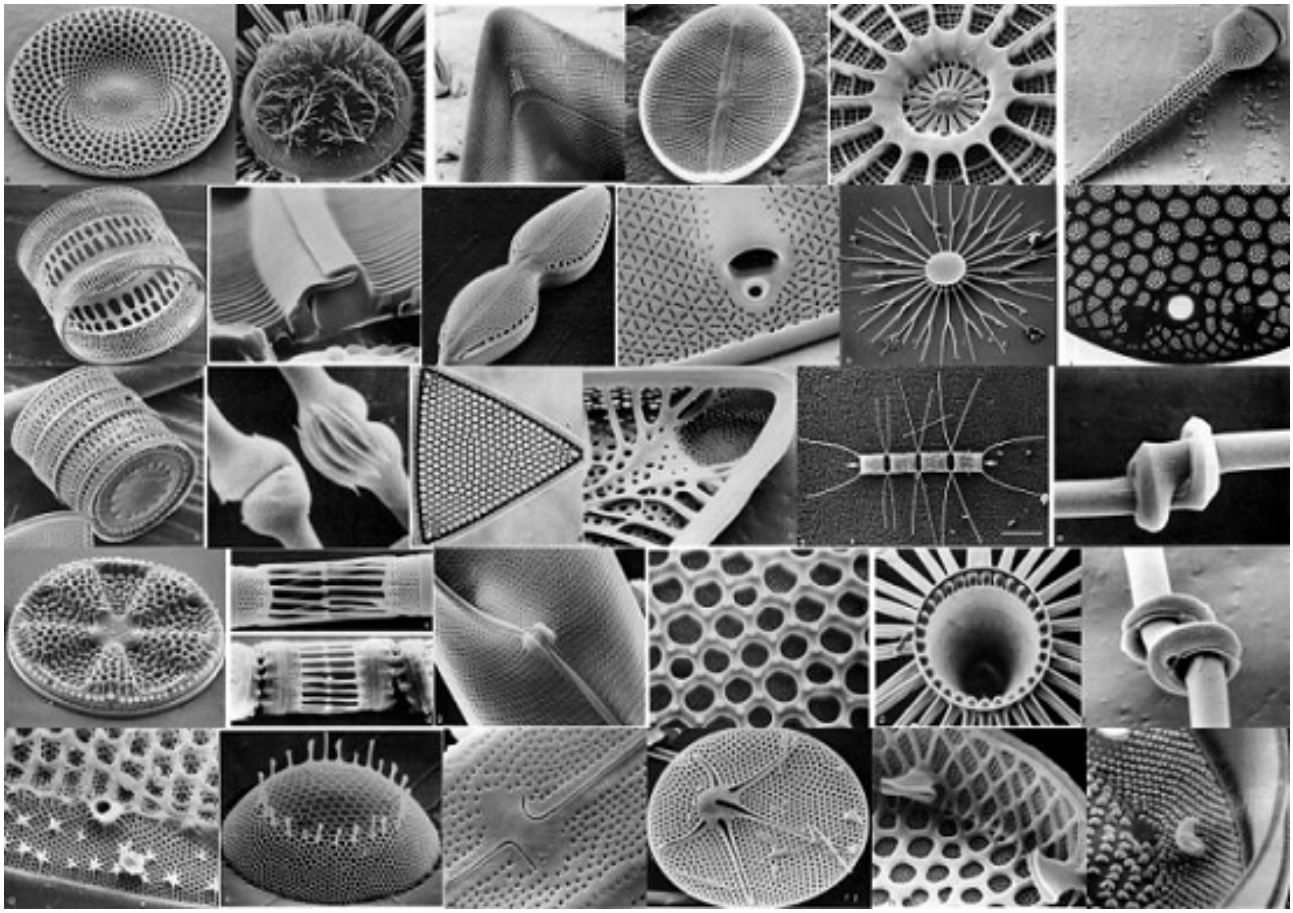

Figure 1-1. Collage Illustrating the Diversity of Diatom Morphologies

In this work, silica-based frustules of Aulacoseira diatoms were utilized as transient bioscaffolds for establishing the shapes of various coatings. Representative scanning electron microscope images of the diatom frustules, (obtained as diatomaceous earth filter material from a local vendor) used as transient scaffolds in this work are shown in Figure 1-2. Native diatom silica is amorphous. However, the processed diatomaceous earth used in these experiments has been flame polished. Flame polishing is done by diatomaceous earth processors to decrease the surface area which prevents silicosis, a respiratory disease caused by inhaling extremely fine silica. This is done for consumer safety, since many commercial applications of diatoms involve direct consumer contact with the powder. Several examples of commercial applications of diatomaceous earth are in pool filters, insecticide, and tooth paste. Flame polishing has three important effects in the context of using diatoms in materials science: surface area is reduced, debris is sometimes welded to the diatoms, and the amorphous silica is partially crystallized. X-ray diffraction shows that the diatomaceous earth used in these experiments contains crystoballite. These frustules possess hollow cylindrical shapes with diameters of 8-12 microns. Some of the frustules possessed an end with a circular hole and a protruding outer rim, as shown in Figure 1-2a. The other end of these frustules was closed and possessed finger-like protuberances. The fingerlike protuberances from one cylinder were often observed to intercalate with those of another to form larger, paired assemblies, as is shown in Fig. 1-2b. Other frustules, such as are shown in Figures 1-2c and 1-2d, were observed to have closed ends. The sidewalls of the Aulacoseira frustules contained mesoscale pores (i.e., with diameters of several hundred nanometers) arranged in rows running parallel to the cylinder length.

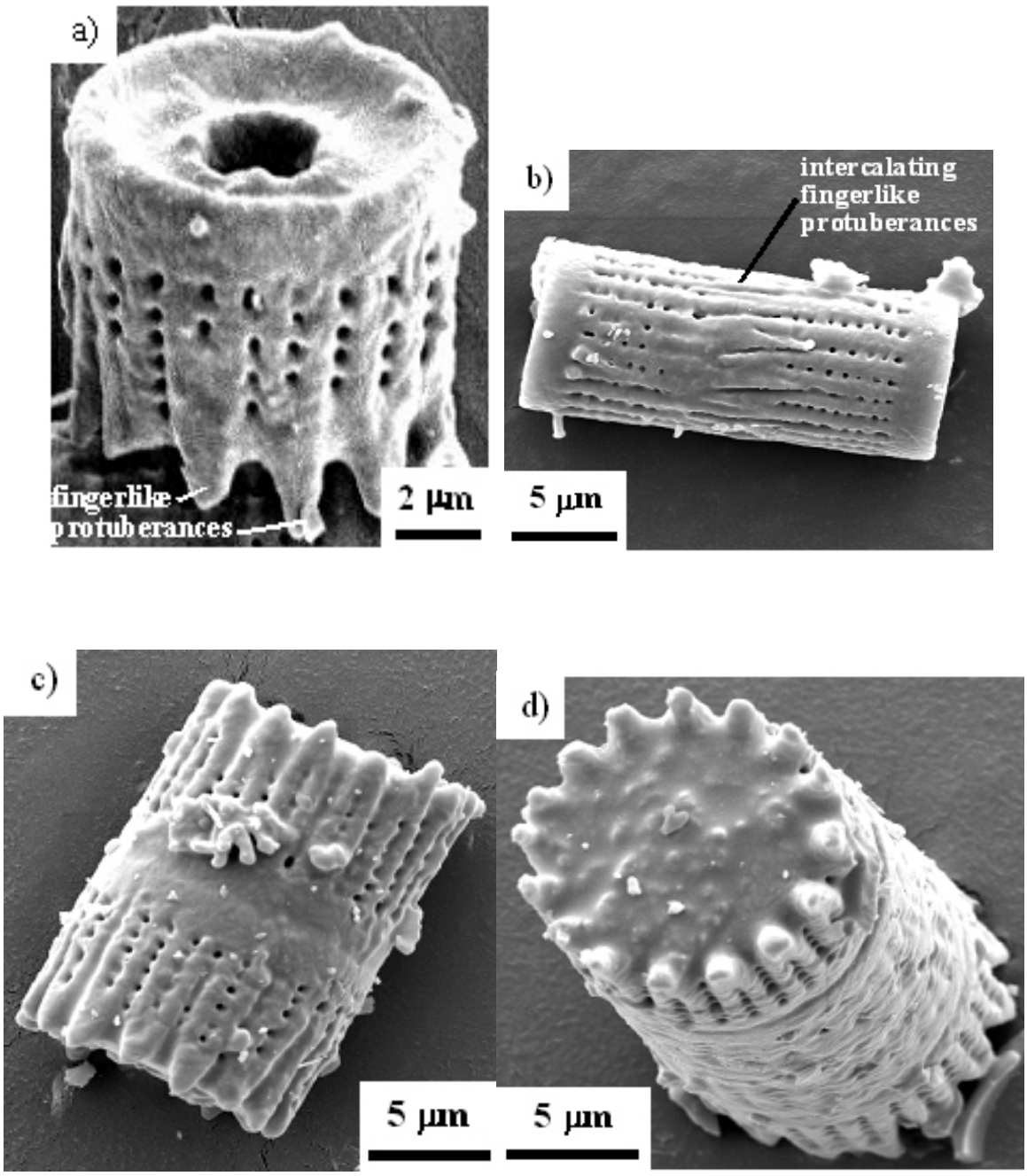

Figure 1-2. SEM images of Aulocaseira Frustules from Diatomaceous Earth.

Chapter 2

Polymer Coating

Polymer coatings were applied by immersing the diatom frustules in polymer precursor solutions. Prior to immersion, the diatom frustules were rinsed with distilled water and acetone to remove residual salts and/or oils. One gram of the diatom frustules was then added to 30 ml of a solution of 5 wt% phenolic resin (RESI-LAM, Georgia-Pacific Chemical Products Corp., Atlanta, GA) dissolved in ethanol. After stirring for 1h, the diatoms were removed from the resin-bearing solution by filtration and the ethanol was allowed to evaporate at room temperature for 1 h. One gram of phenolic-coated diatoms was then immersed in 30 ml of an aqueous solution containing 2 wt% of a cross-linking agent (hexamethylenetetramine, Alfa Aesar, Ward Hill, MA). After stirring for 1 h, the diatoms were removed from the solution and then allowed to cure in an oven at 170^{o}C for 12 h. The coated frustules were then immersed in an aqueous solution containing 49 wt% hydrofluoric acid in order to selectively dissolve the underlying silica from the coating (note: upon removal of the silica, the specimens were observed to float in the HF solution). After washing with distilled water, the specimens were dispersed in ethanol and then applied by dropper to an electron microscope stub. After allowing the ethanol to evaporate, the specimens were coated with a thin layer of gold to avoid charging in the electron microscope. A representative secondary electron image of a freestanding structure generated from this process is shown in Fig. 2-1a. Application of a thin, continuous polymeric coating to the internal and external surfaces of the diatom frustule wall, and along the 10^2 nm diameter pore channels passing through the frustule wall, followed by complete dissolution of the silica, should have yielded a hollow

cylindrical structure comprised of concentric polymer cylinders connected by 10^2 nm diameter struts (i.e., with the struts formed at the locations of the pore channels).

Although the structure shown in Fig. 2-1a possessed a cylindrical shape, the external surface morphology of the starting diatom frustule was not fully preserved. That is, while a continuous polymer coating appears to have been applied to the internal surface and to the mesoscale pore channels running through the wall of this hollow cylindrical frustule (i.e., the struts seen in Fig. 2-1A), the external frustule surface was only partially coated. A fracture section of a similarly coated frustule revealing such partial external coverage is shown in Fig. 2-1B.

To improve the continuity of the external coating, several changes were made to the process. The coating solution was changed to a two-part, 5 min curing epoxy mixture (Loctite® Quick Set™ Epoxy Gel, Henkel Consumer Adhesives, Inc., Avon, OH). 10 wt% of this quick-curing epoxy mixture was dissolved in acetone. One gram of diatom frustules was then added to 30 ml of this epoxy/acetone solution. The mixture was stirred for 15 minutes and the diatom frustules were then removed from the solution by filtration. The acetone was allowed to evaporate, and the epoxy coating was allowed to cure at room temperature. The silica was then selectively removed, as discussed above, in a 49 wt% HF solution. A representative secondary electron image of the resulting specimen is shown in Fig. 2-2A. With this coating approach, continuous coverage of the internal and external surfaces was achieved. However, in this case the epoxy coating was sufficiently thick that the mesoscale pores were completely filled in and covered over. The continuous coating and the filled pores are clearly revealed in the secondary electron images of a partially fractured specimen shown in Figs. 2-2B and 2-2C.

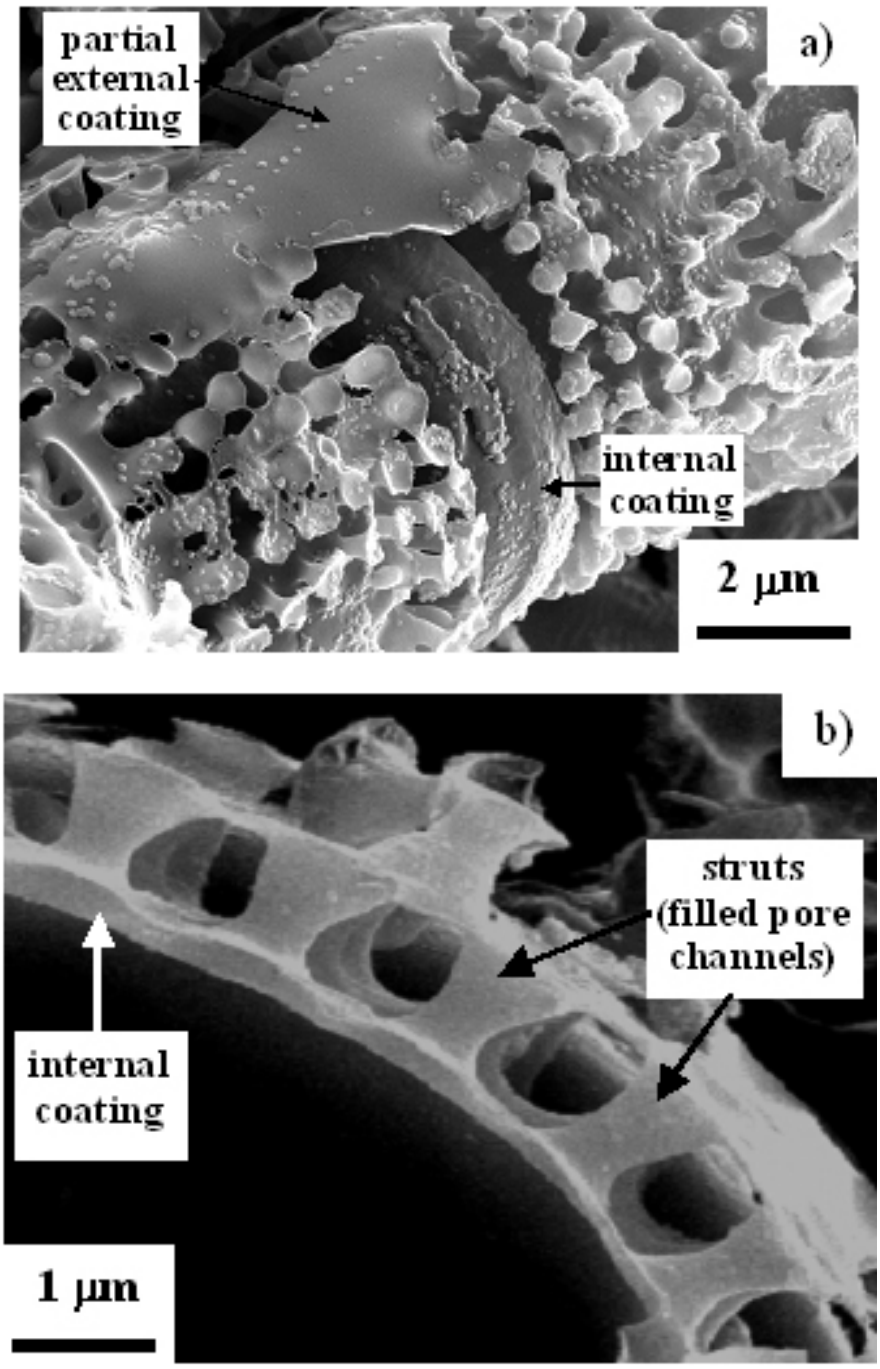

Figure 2-1. SEM Images of 5wt% Phenolic Diatoms

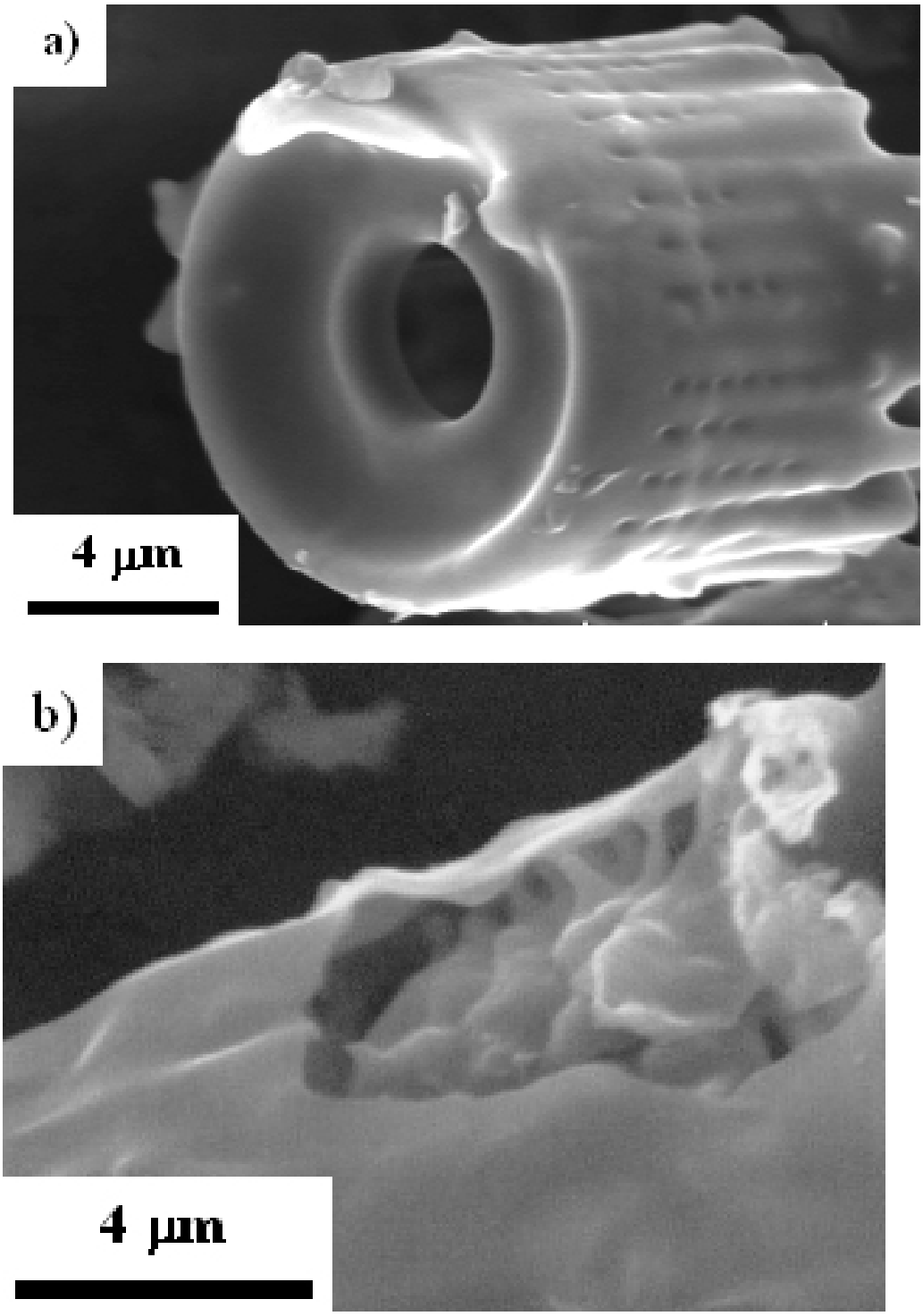

Figure 2-2. SEM Images of 10wt% Phenolic Diatoms

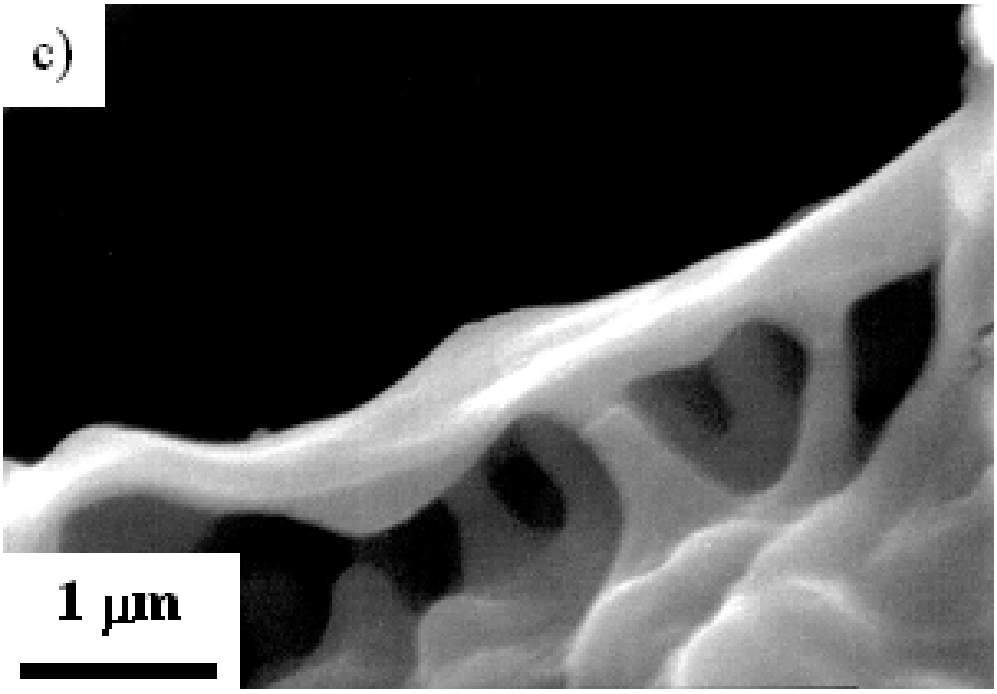

Figure 2-2 continued. SEM Images of 10wt% Phenolic Diatoms

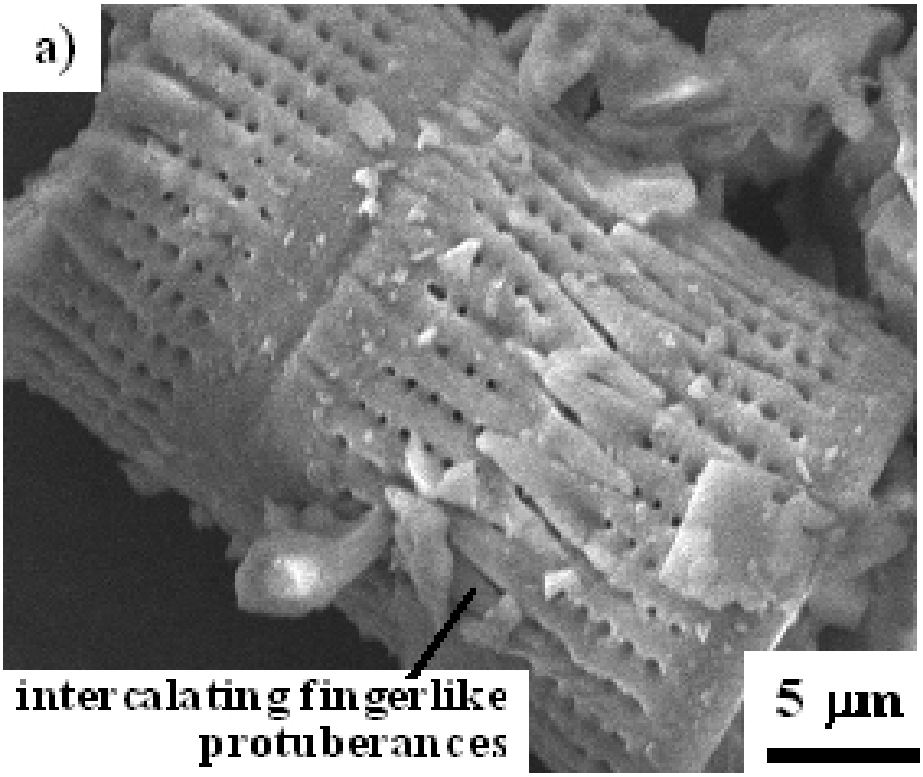

Figure 2-3 continued. SEM Images of 7wt% Epoxy Diatoms

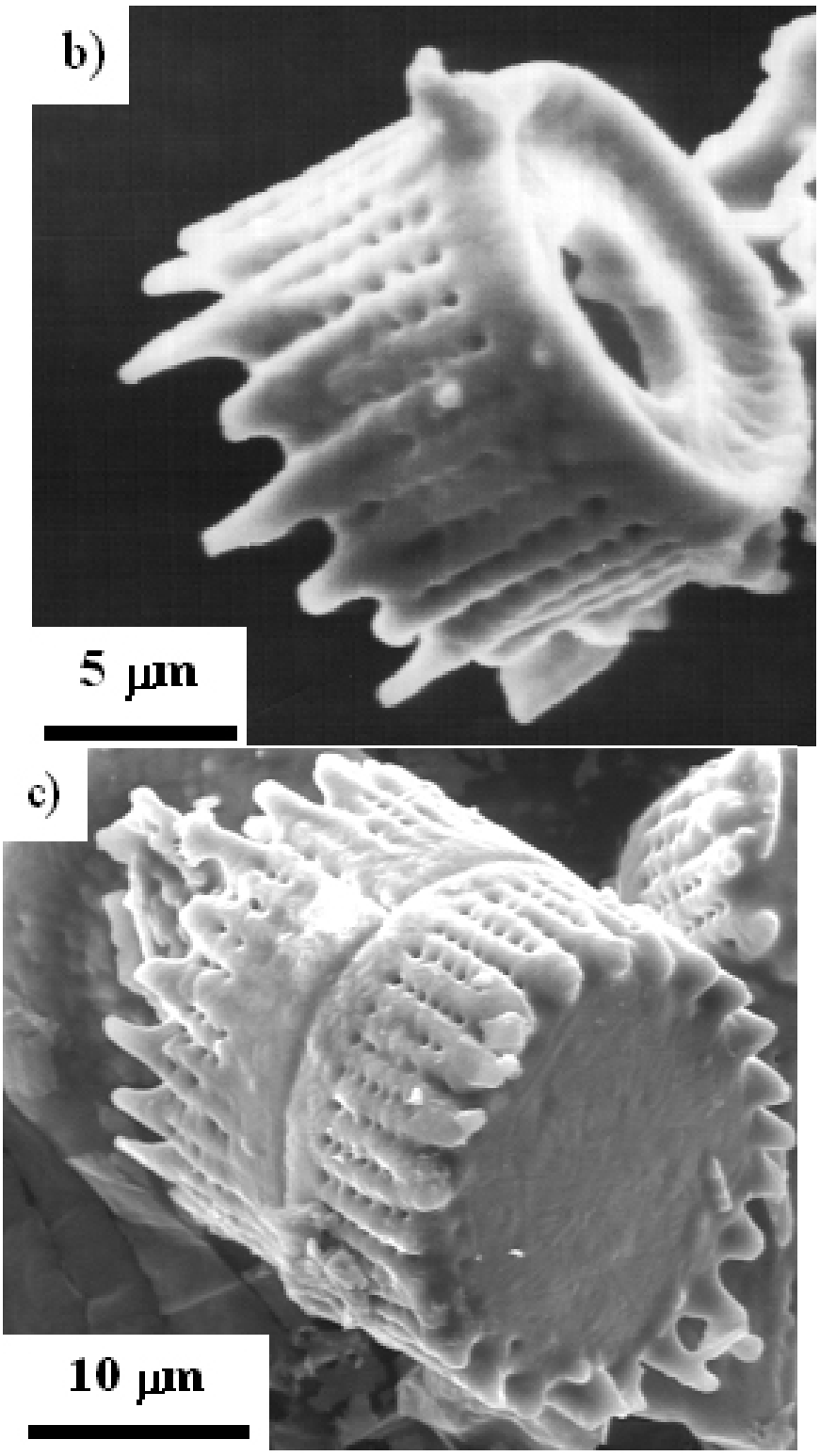

Figure 2-3 continued. SEM Images of 7wt% Epoxy Diatoms

In order to decrease the coating thickness, the concentration of the epoxy in the solution with acetone was reduced from 10 wt% to 7 wt%. A secondary electron image of an as-coated frustule (prior to silica dissolution) is shown in Fig. 2-3A. With the use of a more dilute epoxy solution, the fine features (mesoscale pores, intercalating finger-like extensions) were well preserved. Subsequent dissolution of the silica in the HF solution yielded the epoxy structures shown in Figs. 2-3B and 2-3C, which were quite similar in morphology to the starting frustule structures shown in Figures 1-2a and 1-2c. Thermogravimetric (TG) analyses were conducted on these specimens in air at a heating rate of 10^{o}C/min (TGA 7, Perkin Elmer Inc., Boston, MA). TG analysis of the coated specimens prior to silica dissolution (Fig. 2-4a) revealed that the epoxy coating comprised 28.6% of the weight of the specimen. After exposure of the silica to the HF solution, TG analysis (Fig. 2-4b) confirmed that all of the silica had been removed since the weight loss was nearly complete. EDX analyses of a starting diatom frustule and an epoxy replica are shown in Figs. 2-4C and 2-4D, respectively (note: both specimens were coated with gold to avoid charging in the electron microscope). The presence of a strong carbon peak in Fig. 2-4D, and the loss of the strong Si peak relative to Fig. 2-4C, were consistent with the conversion of the silica-based diatom frustule into an epoxy replica (the aluminum peaks and the small silicon peak in Figs. 2-4C and 2-4D were generated by the aluminum alloy stub onto which the specimens were placed; the small fluorine peak in Fig. 2-4C was a result of residual fluorine from HF treatment). This work demonstrates that freestanding microscale polymeric structures with complex 3-D shapes and nanoscale features may be synthesized by using the frustules of self-replicating diatoms as transient scaffolds.

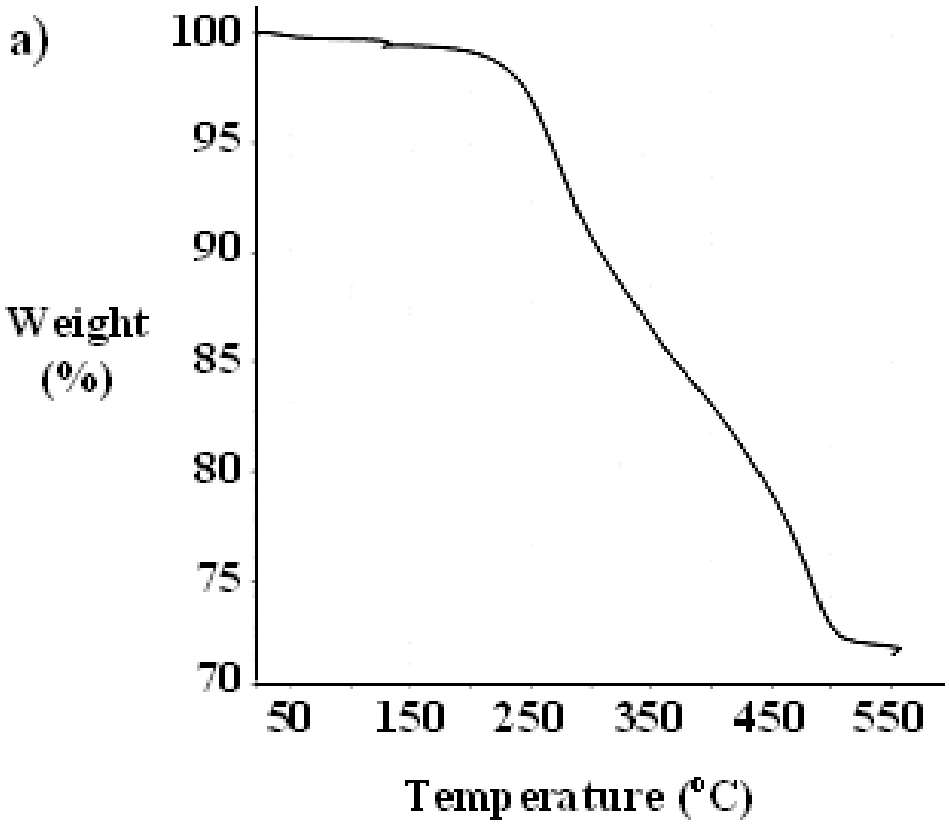

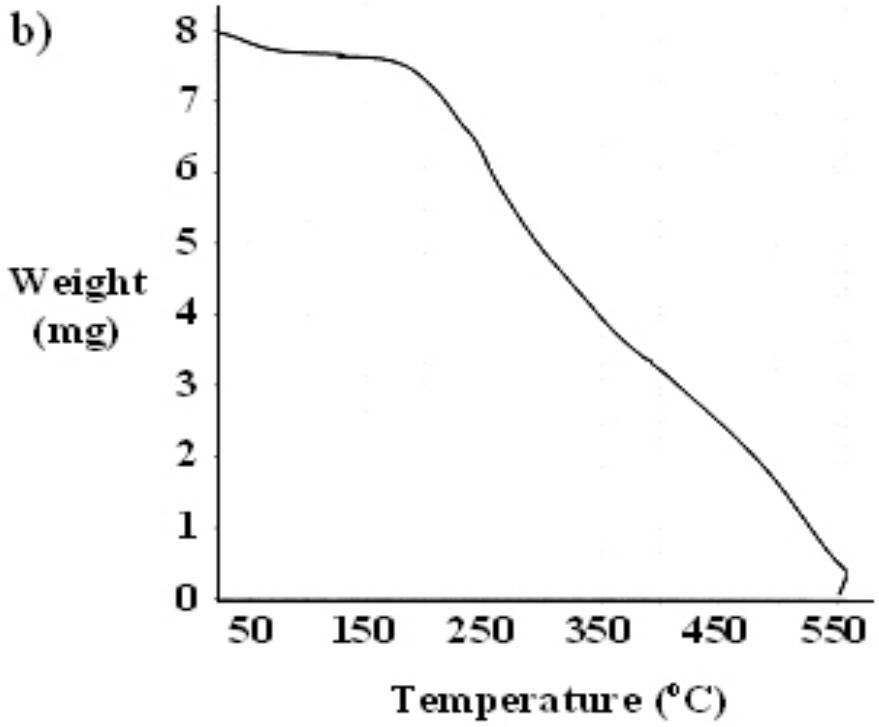

Figure 2-4. TGA and EDS Analysis of Epoxy Diatoms

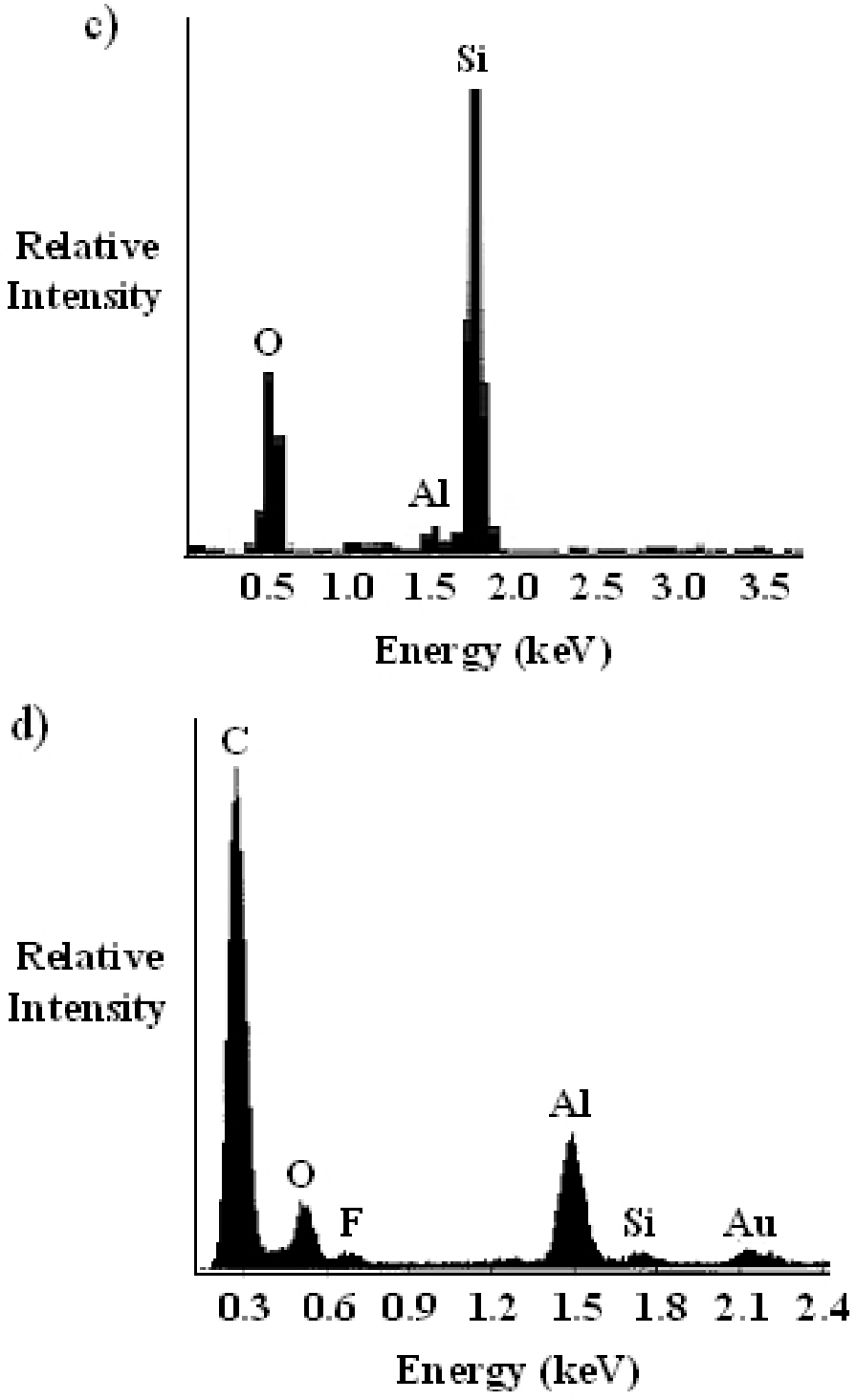

Figure 2-4 continued. TGA and EDS Analysis of Epoxy Diatoms

Although a wide variety of frustule shapes exist among the various diatom species, the coating process described in this paper is not limited to the use of only these bioclastic structures. Nature provides numerous other self-replicating biomineralized micro/nanostructures with multifarious 3-D shapes (e.g., the microshells of coccolithophorids, silicoflagellates, radiolarians, sponges, bacteria, etc.[15-18,28]) that may be utilized to generate polymer structures of desired morphology. Furthermore, the genetic engineering of diatoms or other biomineralizing organisms may lead to a variety of replicable bioscaffolds with non-natural shapes (note: towards this end, the genome of a diatom, *Thalassiosira pseudonana*, has recently been mapped[29]). The chemistries of the structures generated by the present process are also not limited to phenolic resin-based or epoxy-based compositions. A variety of organic micro/nanostructures may be generated from bioclastic scaffolds provided that: i) a dilute solution of the organic material, or a precursor to the organic material, can be dissolved in a volatile solvent, ii) a continuous organic film can be produced by infiltration of the solution into the scaffold and then evaporation of the solvent, and iii) the underlying bioclastic scaffold can be selectively removed from the organic coating (e.g., by selective dissolution in an acidic solution). For the latter requirement, the organic coating must remain intact as the bioclastic scaffold is removed, which may necessitate an additional processing step (e.g., cross-linking of a polymer coating prior to dissolution of the scaffold). Unlike other approaches for fabricating 3-D polymeric micro/nanostructures, this solution-based bioscaffold coating process does not require expensive patterning facilities or reaction processing equipment and is highly scalable. The bioscaffolds may also be cultured in large quantities. Indeed, large-scale diatom cultivation is currently used in aquaculture

operations (i.e., diatoms provide a food source for the commercial production of clams, oysters, scallops, shrimp, and several fish species)[30]. Scale up of the present process could enable the generation of large quantities of inexpensive, 3-D polymer micro/nanostructures for use in a host of biomedical, agricultural, cosmetic, environmental, chemical/catalytic, microfluidic, gas sensing, photonic, and aerospace applications[1-14].

Chapter 3

Zirconia Coating

Nature provides spectacular examples of mineralized nanoparticle assemblies with complex, three-dimensional (3-D) shapes that are replicated with fidelity in large numbers. Unfortunately, the limited natural chemistries of such bioclastic structures hinder their use in nanotechnology. This work shows for the first time, how such self-replicating structures can be converted into synthetic, alkoxide-derived nanocrystalline materials without a loss of 3-D shape or fine features. Silica-based diatom microshells (frustules) were coated with a continuous layer of sol-gel-derived nanocrystalline zirconium oxide. Predominantly tetragonal or monoclinic zirconia could be produced by controlling heat treatment conditions. Selective silica dissolution then yielded freestanding, frustule-shaped nanocrystalline zirconia micro-assemblies with well-preserved nanoscale features. This simple process enables attractive characteristics of biology (genetically-precise, massively-parallel replication of 3-D bioscaffolds) and synthetic chemistry (low-temperature conversion into functional nanocrystalline materials) to be coupled to yield large numbers of 3-D nanocrystalline assemblies with tailored chemistries, complex shapes, and nanoscale features for numerous applications.

Aulacoseira frustules (Figure 3-1) were first immersed in a boiling ammonium hydroxide solution (pH = 10) for 4 h in order to hydrolyze the silica surfaces. After filtration from this solution and drying at room temperature, the frustules were exposed to a solution of zirconium n-propoxide (70 wt% in 1-propanol, Aldrich Chemical Co., Milwaukee, WI) with anhydrous ethanol, concentrated (29%) ammonium hydroxide, and

deionized water (the solution possessed a molar $Zr(OC_3H_7)_4$:NH_4OH:H_2O:EtOH ratio of 1.0:0.67:3.36:480).

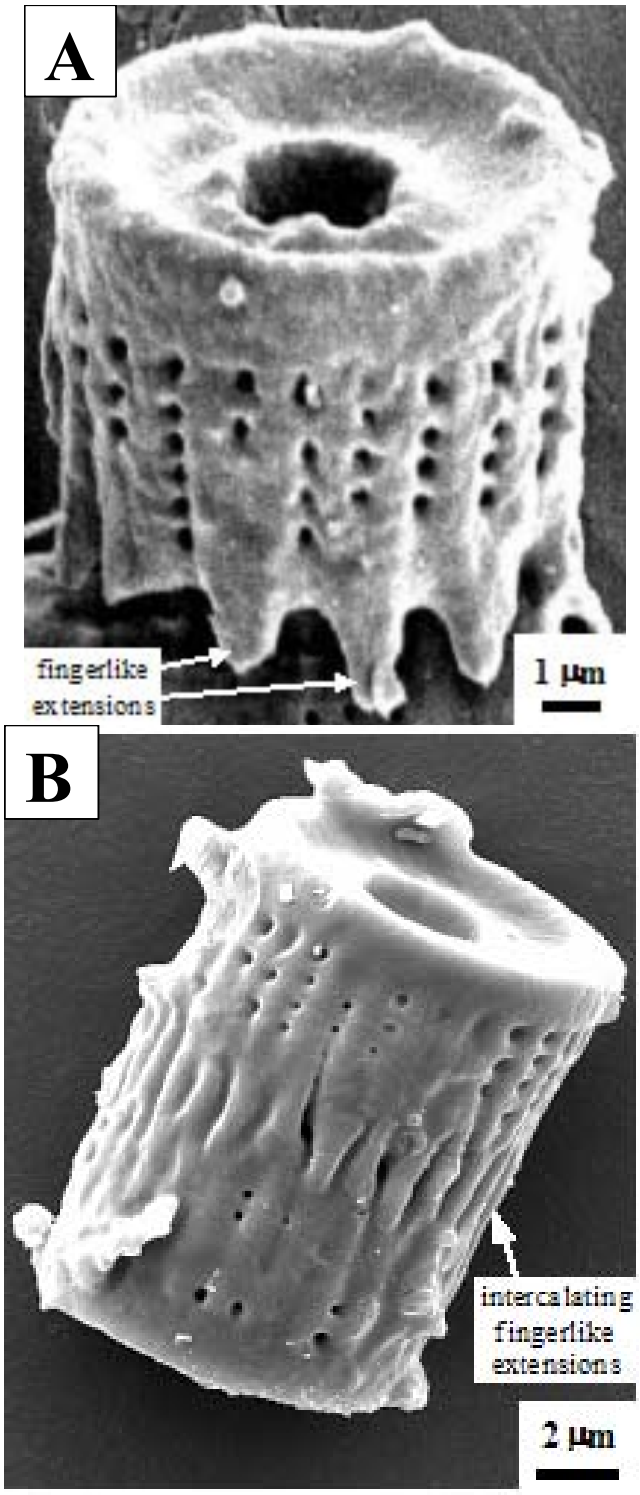

Figure 3-1 SEM Images of Aulocaisera Diatom Frustules.

0.4 grams of hydrolyzed diatom frustules were then added to 20 ml of this solution. The mixture was stirred and refluxed for 3 h at 76°C. 8 ml of the solution was then allowed to evaporate at 66°C. The mixture was stirred and refluxed for an additional hour, after which 5 ml more of the solution was allowed to evaporate. After conducting a final step of stirring and refluxing for 2 h, the solution was allowed to completely evaporate at 56°C in air. The coated frustules were collected and fired in air at 550-850°C for 3 h. The silica in the zirconia-coated frustules was then selectively removed by immersion for 2 h in an aqueous 30 wt% sodium hydroxide solution at 85°C.

The surface morphologies of the starting diatom frustules, and of the resulting zirconia structures, were evaluated with a field emission gun scanning electron microscope (FEG-SEM, Model XL-30, Philips Electron Instruments, Eindhoven, The Netherlands). X-ray diffraction analysis (PAD-V diffractometer, Scintag, Sunnyvale, CA) was used to evaluate the phase content of the zirconia structures and the average crystallite size (through the use of the Scherrer equation)[22]. The internal morphology of the zirconia structures was revealed with the use of a dual beam, focused ion beam instrument (Model Strata DB-235 System, FEI Company, Hillsboro, OR). Ion-milled cross-sections were examined with transmission electron microscopy (TEM, Model CM-200T, Philips Electron Instruments). The scanning electron microscope and transmission electron microscope were both equipped with a Si/Li energy-dispersive x-ray (EDX) detector (Edax International, Mahwah, NJ) for local chemical analyses. Secondary electron images of the resulting free standing structures generated after firing at a peak temperature of 650°C for 3 h are shown in Figures 3-2a and b. These structures retained the cylindrical shapes and fine features of the starting silica-based frustules. The

mesoscale pores on the sidewalls, and the fingerlike extensions on the closed ends of the frustules, were clearly preserved in the converted structures (note: structures with similar shapes and fine features were also observed after the 550°C and 850°C treatments).

A secondary electron image of an ion-milled cross-section obtained near the open end of a converted frustule is shown in Figure 3-2c (note: although ion milling removed some of the protruding rim from the open end of this frustule, the hole at this end can be clearly seen). This cross-section revealed that the coating was continuous and possessed a thickness of 0.2-0.6 μm. Energy-dispersive x-ray analyses at various locations through this cross-section (such as shown in Figure 3-2d) revealed distinct peaks for zirconium and oxygen, but not for silicon, which confirmed that the silica had been completely removed by selective dissolution in the sodium hydroxide solution (note: the carbon peak was a result of the carbon tape the converted frustules were mounted on to avoid charging by the electron beam in the electron microscope). X-ray diffraction patterns obtained from the converted structures after firing at peak temperatures of 550°C, 650°C, or 850°C for 3 h are shown in Figures 3-3a, 3-3b, and 3-3c, respectively. The presence of zircon ($ZrSiO_4$), or residual crystalline silica (as quartz, cristobalite, or tridymite) were not detected by x-ray diffraction analyses after any of the firing and dissolution treatments.

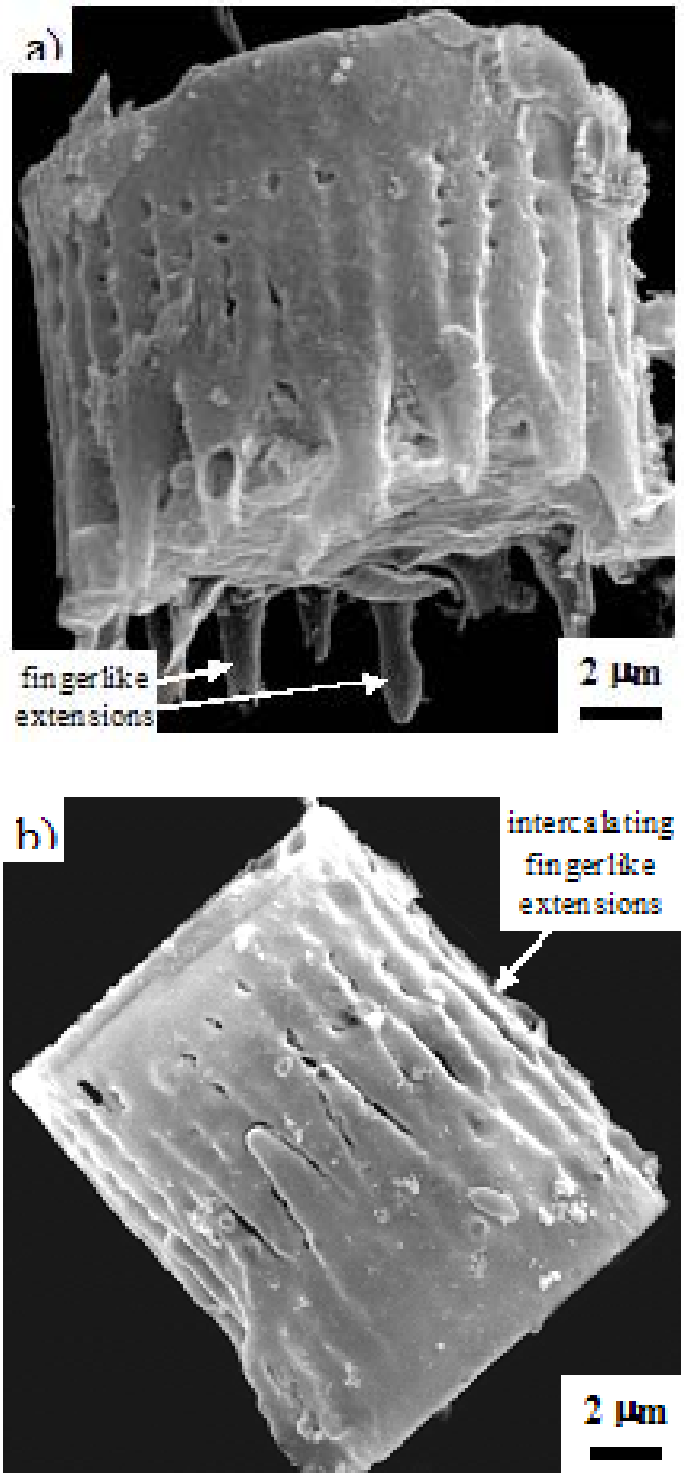

Figure 3-2 SEM Images of Free Standing Ziroconia Frustules

The predominant phase present after firing at 550°C was tetragonal zirconia, with a small amount of monoclinic zirconia also detected. With increasing firing temperature, the relative amount of monoclinic zirconia increased.

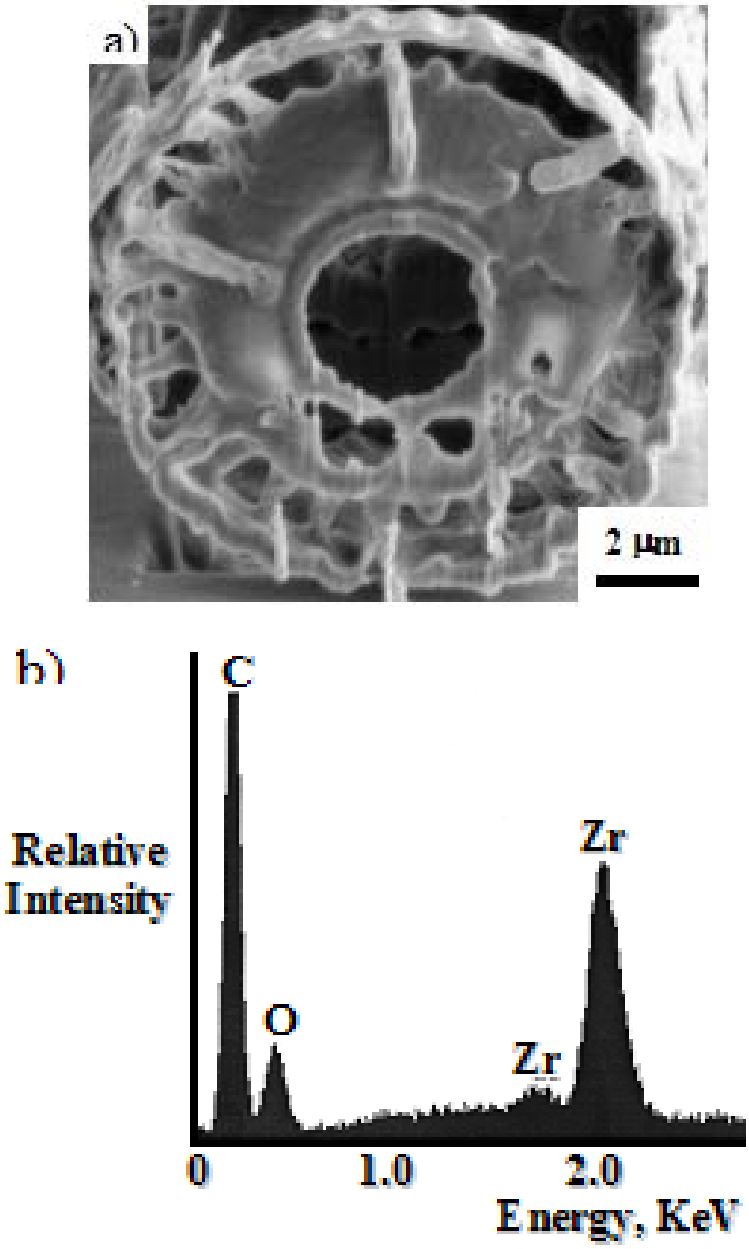

Figure 3-3 SEM Image and EDS Spectra of ZrO_2 FIB Cross-section

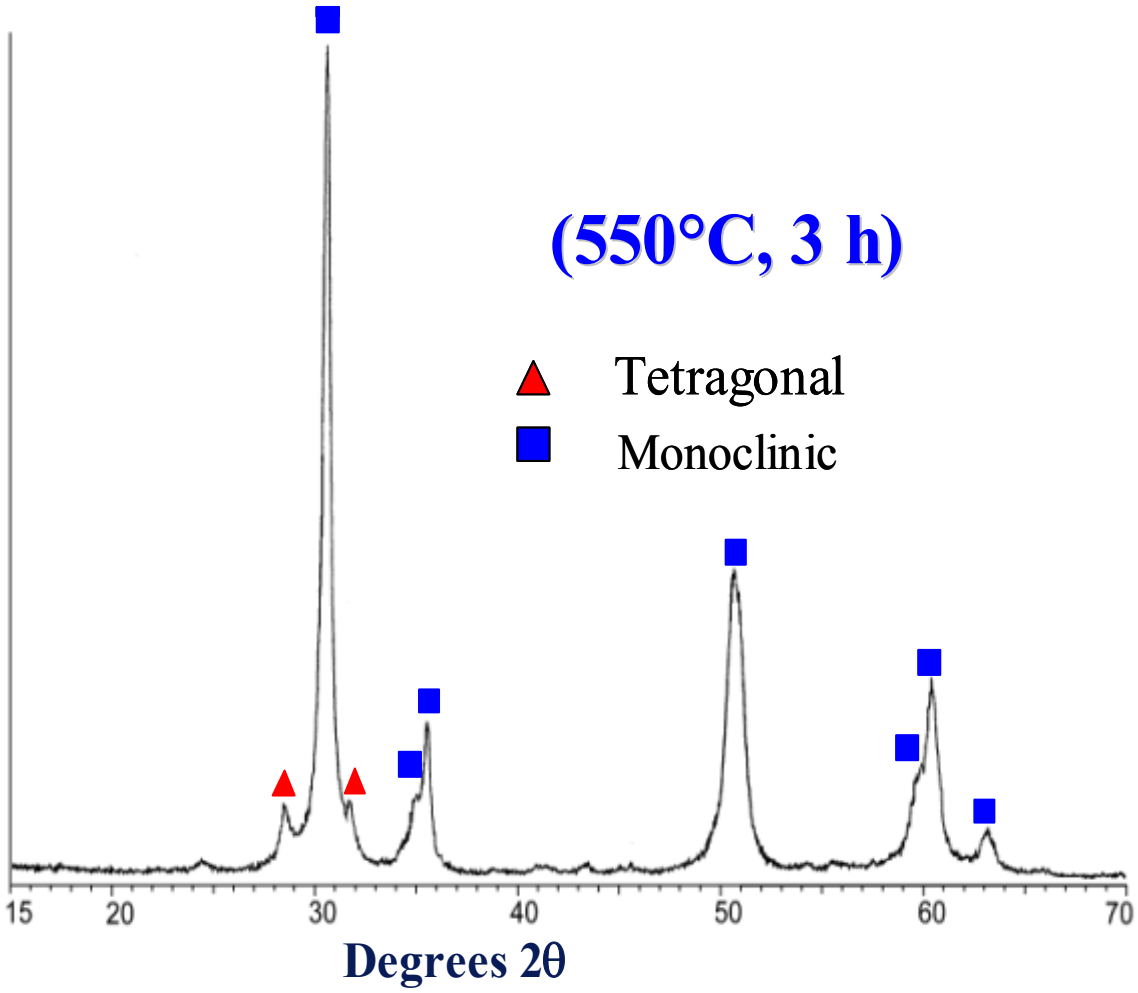

Figure 3-4 X-ray diffraction pattern of the zirconia sample fired at 550°C

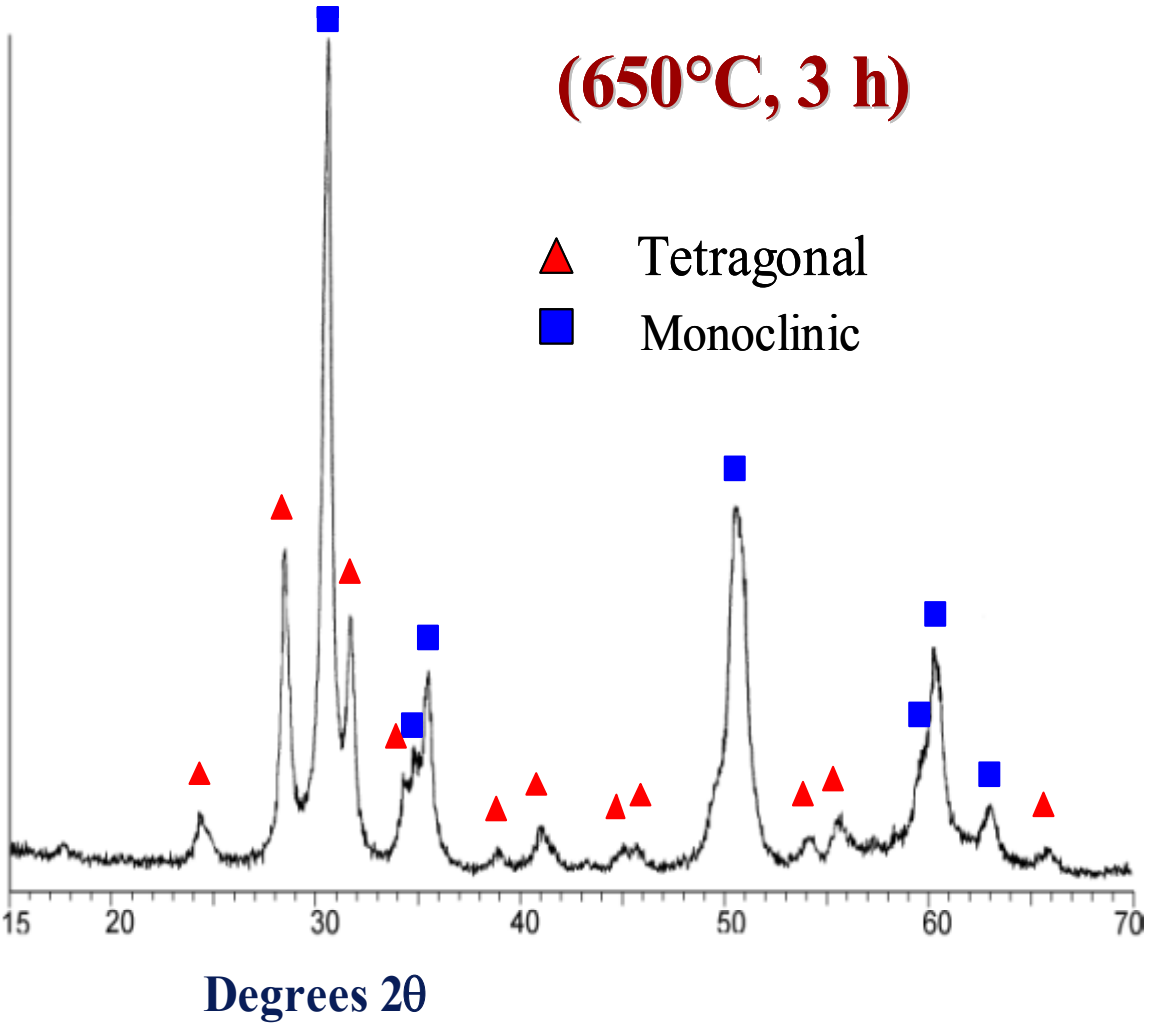

Figure 3-5 X-ray diffraction pattern of the zirconia sample fired at 650°C

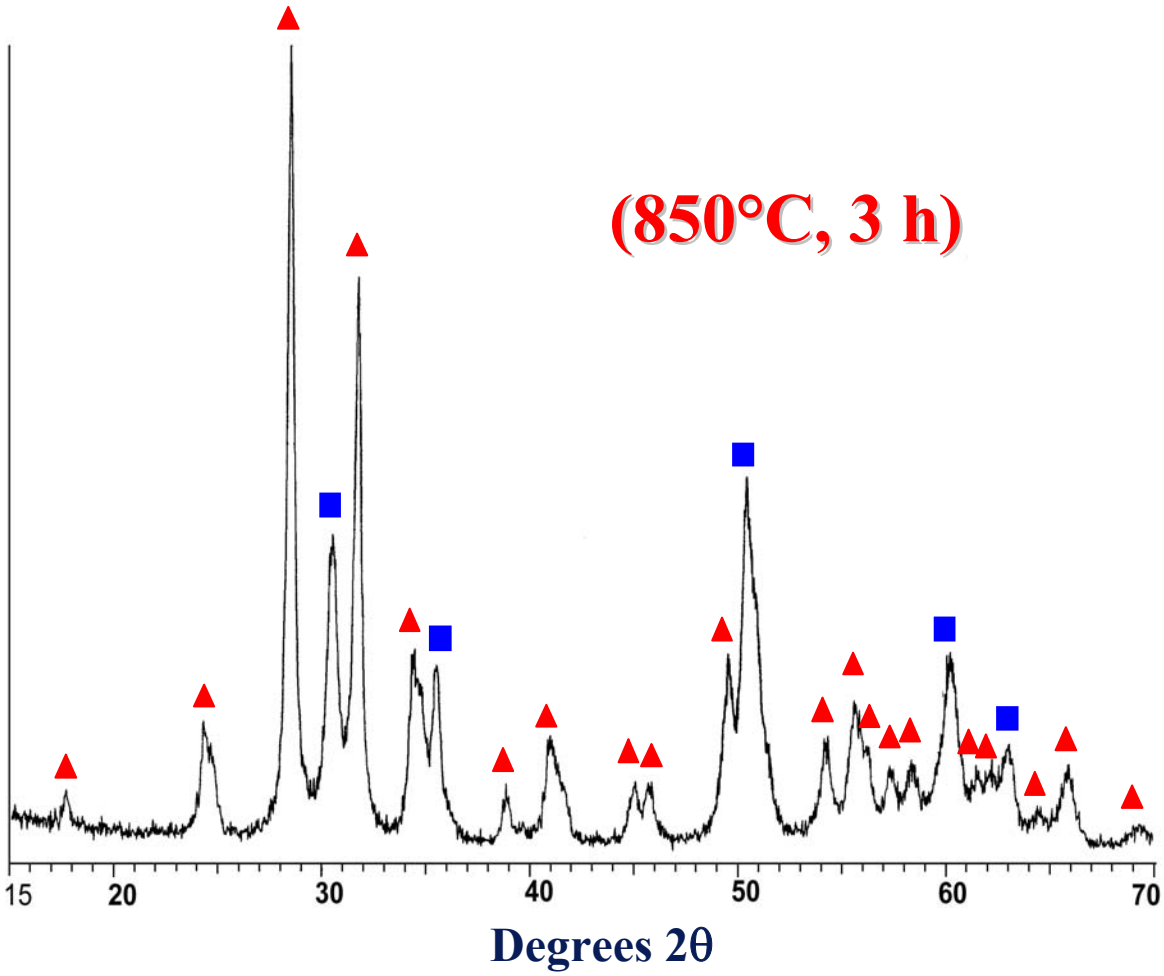

Figure 3-6 X-ray diffraction pattern of the zirconia sample fired at 850°C

After the 850°C treatment, monoclinic zirconia became the predominant phase. The formation of nanocrystalline tetragonal zirconia in advance of the monoclinic zirconia polymorph during the firing of sol-gel-derived coatings at <850°C has been reported by a number of authors.[19-21] The widths of the most intense diffraction peaks for tetragonal zirconia (the (101) peak located near 2θ = 30 degrees in Figure 3-4) and for monoclinic zirconia (the (-111) peak located near 2θ = 28 degrees in Figure 3-5) were measured after the 550°C and 850°C heat treatments, respectively. Insertion of these values into the Scherrer equation yielded average crystallite sizes of 47 nm for tetragonal zirconia after 550°C and 42 nm for monoclinic zirconia after 850°C[22]. A dark field TEM image confirming the nanocrystalline structure of a converted frustule (after reaction at 650°C for 3 h) is shown in Figure 3-7A. Electron diffraction analysis of this specimen (Fig. 3-7B) revealed diffraction rings consistent with a mixture of tetragonal and monoclinic zirconia, in agreement with the XRD analysis in Figure 3-6. The present work provides the first demonstration that nanocrystalline micro-assemblies with tailorable, sol-gel-derived compositions can be generated with 3-D shapes and nanoscale (10^2 nm) features derived from self-replicating, nanoparticle-based bioclastic assemblies. The ability to change the chemistry of such 3-D assemblies, without altering the shapes and nanoscale features, enables such structures to be endowed with a much broader range of properties than are exhibited by biogenic silica or calcium carbonate. For example, 3-D micro-assemblies of nanocrystalline zirconium oxide could be used for rapid catalysis, low-temperature gas sensing, minimally invasive biomedical devices, and controlled-shape reinforcements in composites.

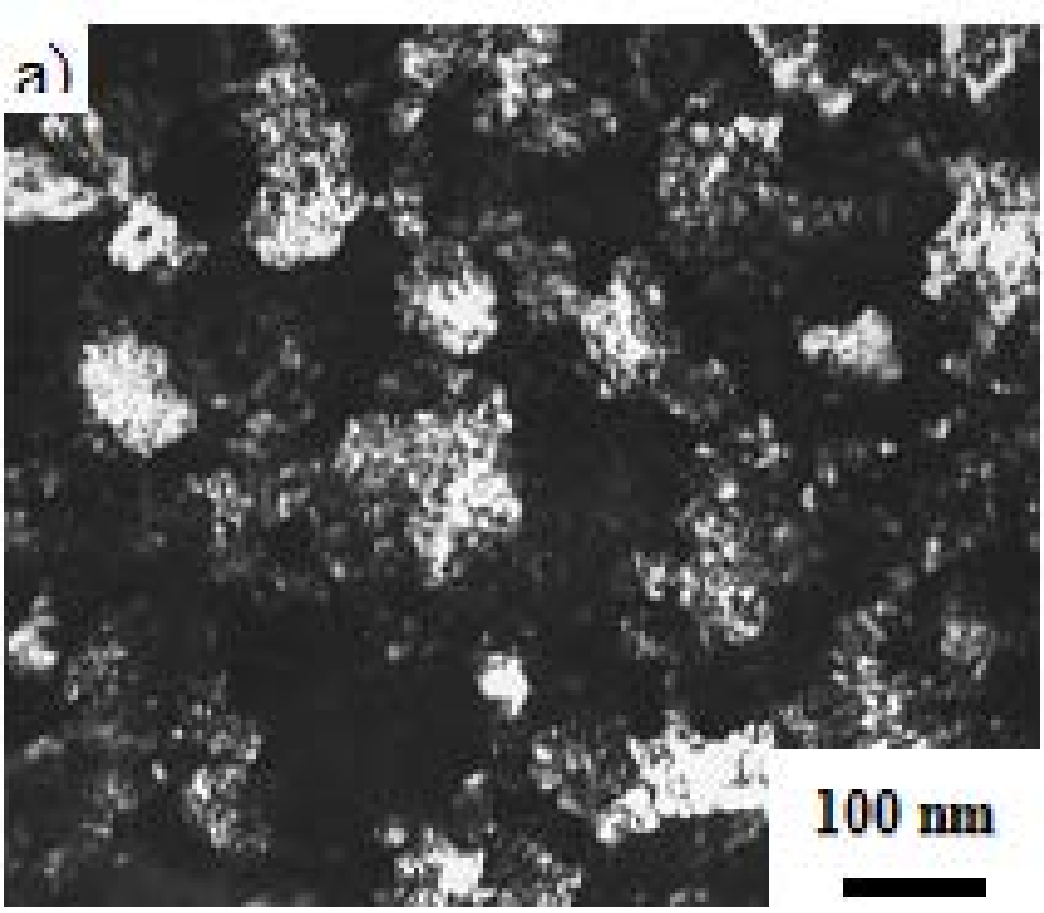

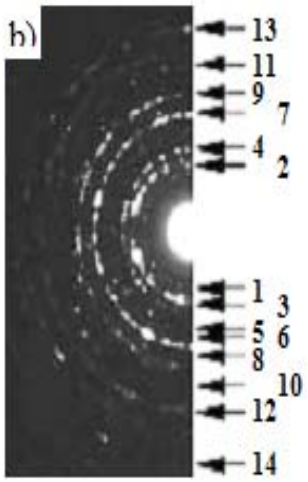

c)

Ring No.	Calculated d value	Corresponding (hkl)
1	3.687	$(110)_M$
2	3.164	$(-110)_M$
3	2.985	$(101)_T$
4	2.570	$(110)_T$
5	2.174	$(-121)_M$
6	1.990	$(-202)_M$
7	1.812	$(200)_T/(022)_M$
8	1.631	$(031)_M$
9	1.542	$(131)_M$
10	1.325	$(-223)_M$
11	1.285	$(220)_T$
12	1.178	$(114)_T$
13	1.039	$(321)_T$
14	0.902	$(400)_T$

Figure 3-7 TEM Analysis of 650ºC Sample

Because a wide variety of functional ceramic coatings can be produced by sol-gel and other synthetic organic precursor routes, the present process may be used to convert diatom frustules into a host of other chemically-tailored nanocrystalline assemblies with attractive electronic, magnetic, optical, chemical/biochemical, or mechanical performance. Although the natural diversity in diatom frustule shapes is considerable, it seems possible, if not likely, that genetic engineering could be used to produce an even greater range of tailored shapes and fine features. Indeed, initial steps have been taken in this direction.

Transformation based approaches have been developed for introducing and expressing genes in diatoms, and a diatom genome (Thalassiosira pseudonana) has recently been sequenced[27-29]. While genes influencing the frustule shape and fine features remain to be identified, the potential exists for genetic modification of diatoms to yield frustules with tailored shapes and fine features. Such viable, genetically engineered diatoms could then be cultured to yield large quantities of similarly shaped frustules that, in turn, could be converted by the present process into desired functional chemistries. The present process may also be applied to bioclastic micro-assemblies generated by numerous other types of algae, bacteria, fungi, or other microorganisms[31-33]. The multifarious combinations of natural or genetically modified bioclastic shapes and synthetic chemistries that may be utilized in this hybrid process could yield a diverse spectrum of micro-devices (sensors, actuators, transducers, filters/membranes, reactors, capsules, fillers/reinforcements, etc.) for telecommunications, transportation, biomedical, environmental, petrochemical, energy production/storage, and defense applications.

Chapter 4

SiC via Kion Polysilazane Coating

Diatom frustules are very uniform in size and shape and many have geometries that could potentially be useful as MEMS components, controlled size abrasives, high temperature filters, and composite reinforcements. Figure 4-1 shows examples of frustule geometries that could be useful MEMS components. Many of the frustules in these figures potentially be used as microbearings, microcantilevers, microgears, microwheels, microfilters, microblades, and other mechanical components. However, silica is not an ideal candidate material for these types of mechanical structures as the mechanical properties of silica are poor[71]. Silicon Carbide and Silicon Nitride both have excellent mechanical properties that could be useful in diatom geometries[72].

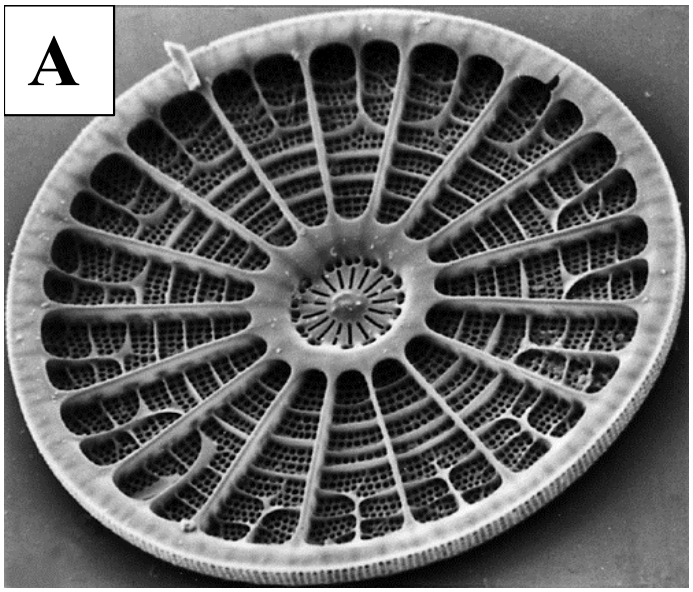

Figure 4-1 Images of potentially useful frustule types for MEMS applications.

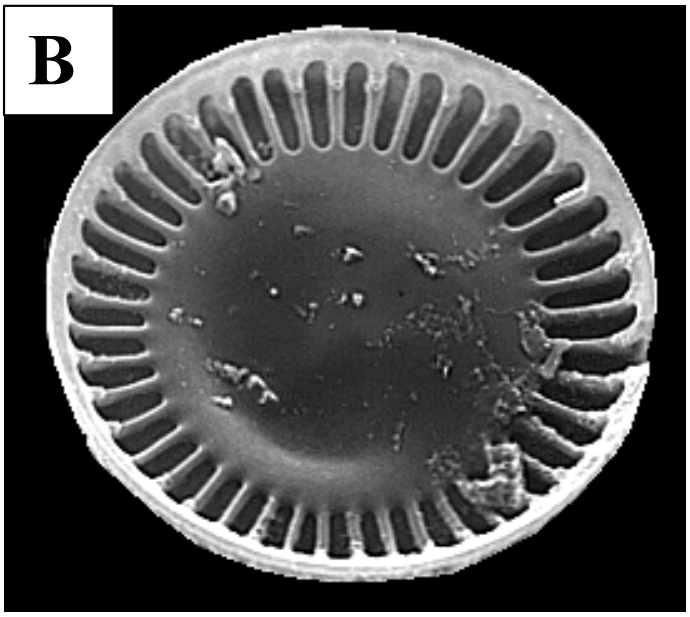

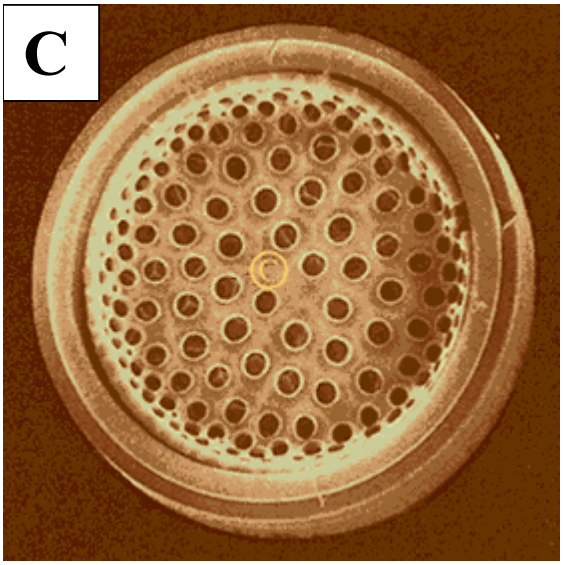

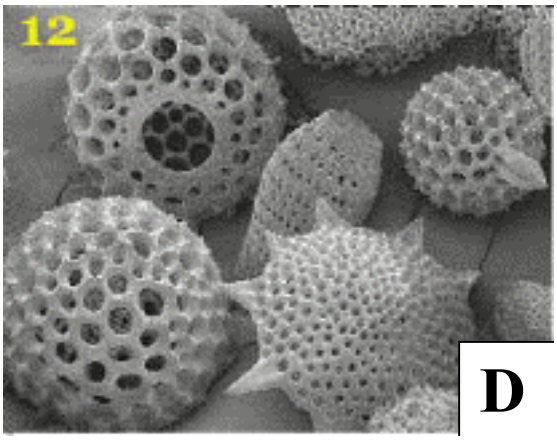

Figure 4-1 continued Images of potentially useful frustule types for MEMS applications.

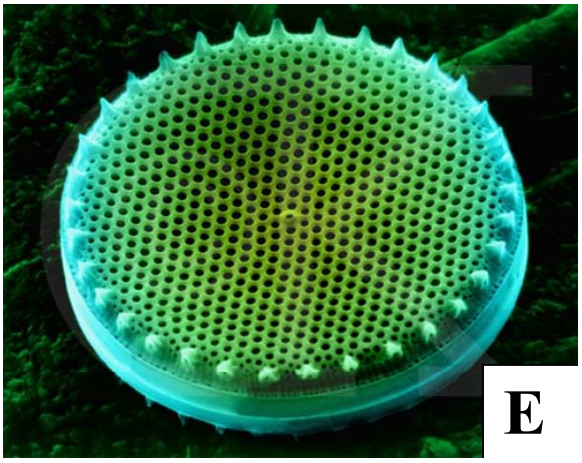

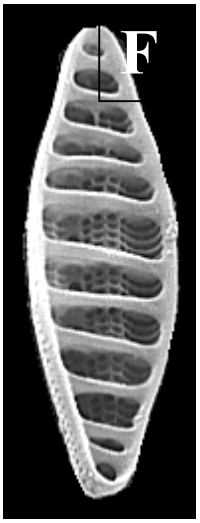

Figure 4-1 continued Images of potentially useful frustule types for MEMS applications.

This research was done in order to determine if a shape preserving coating could be made from a relatively high molecular weight pre-ceramic polymer. Previous coating work had been done using monomer based coatings such as epoxy and zirconium isopropoxide. Due to the much larger persistence length of polysilazane molecules, it was unclear whether a coating could be made to preserve the fine features found in diatom frustules. In this work, diatom frustules were coated with polysilzane, a pre-ceramic polymer, which can be heat-treated to form Silicon Carbide or Silicon Nitride[74]. After coating, the frustules were heat treated to form silicon carbide. For some applications, it may be preferable to have freestanding silicon carbide frustules. This was accomplished by selectively dissolving the silica using a 30wt% sodium hydroxide solution.

Polysilazanes are a class of inorganic polymers with a -Si-N- backbone with a variety of functional groups attached as side groups[73]. Kion-S, the polysilazane used in these experiments, is a relatively high molecular weight amine-terminated polysilazane

with 10wt% solids in a hydrocarbon solvent supplied by Kion Corp (Huntingdon Valley, Pennsylvania, USA). This polysilazane cross-links through its amine groups when allowed to dry in air. When fired in argon, polysilazanes transition from a polymeric state at room temperature, to amorphous silicon carbide at around 1000°C, and to crystalline silicon carbide at 1400-1500°C. If polysilazane is fired in ammonia switching to nitrogen at 700°C, conversion to silicon nitride occurs.

In these experiments, diatomaceous earth was used as the diatom source. The frustules were prepared by washing with DI water followed by acetone. The frustule surfaces were then hydroxylated, by boiling in an ammonium hydroxide solution for four hours. The frustules were dip coated by immersion in a stirred Kion-S for 15min. The frustules were then filtered, separated by spreading the frustules across the filter paper, and cured in a vacuum oven at 125°C. In some cases, a second coating was applied to the frustules after curing, in the same manner. Figure 4-2 shows SEM images of frustules after a single and double polysilzane coating. The images show that the coatings were continuous and partially filled in the diatom pores. Heat treatments were performed to convert polysilazane to amorphous silicon carbide. This was accomplished by firing at 1100°C for 6 hours at a heating and cooling rate of 5°C/min. Argon was used as the firing atmosphere, and titanium foil was used as a getter to remove oxygen impurities. Figure 4-3A shows an SEM image of the fired sample and Figure 4-3B contains an EDS spectrum from this sample. While the coating looks to be continuous, it appears that the pores are more heavily filled in. EDS analysis shows the presence of Si, O, and C in the sample. A gold coating was applied to the samples to prevent charging, and the substrate was an aluminum SEM stub. After dissolving the silica away, SEM and EDS analysis

was again conducted on the sample. Figure 4-4A shows the double polysilazane coated sample fired at 1100°C in argon for 4 hours after treatment with NaOH. It can be seen that after NaOH treatment, shape preservation decreased substantially. Many of the resulting structures were deteriorated from the as coated form. There are several possible reasons for this. The coating may not have been completely continuous which could have caused unconnected fragments to separate from the frustules as the underlying SiO2 was removed. It is also possible that the NaOH solution etched the amorphous silicon carbide coating, although at a slower rate than SiO2. This could have caused thin regions of the coating to be dissolved away damaging the coatings. Alternatively, the silicon carbide may have had small regions with SiO2 impurities that were etched away by the NaOH treatment, resulting in damaged coatings. The EDS spectra found in Figure 4-4B clearly demonstrates that the silica was dissolved. The peak of carbon increased in figure 4-4B relative to 4-4A, while the oxygen and silicon peaks decreased. Gold coating was not used in this case since it was determined that SiC did not charge in the SEM. The aluminum peak seen previously was not observed since the spectrum was taken from the top of a pile of SiC frustules.

In response to the difficulties found in preserving the frustule structure after dissolving away the silica underlying the SiC coatings, a second approach was developed. High quality epoxy replicas have previously been synthesized. The epoxy diatom replicas were used as a substrate on which to coat polysilazane. Figure 4-5A shows an epoxy diatom coated with polysilazane. The coated epoxy diatoms were fired at a heating rate of 2°C/min to 500°C and then at 5°C/min to 100°C and held for 6 hours. Epoxy when fired to 1100°C in argon becomes carbonized, emitting various gasses as it

progresses from epoxy to carbon. The heating rate was slowed to 2°C/min below 500°C to reduce the rate of gas production, in order to limit distortions of the polysilazane as the gasses diffused through the coating. Figure 4-5B and 4-5C show SEM images of the polysilazane/carbon composite diatoms. These images show that the epoxy gasses created increased porosity in the polysilazane coating. The resulting diatom structures are carbon/silicon carbide composite. While these structures are not expected to have good mechanical strength due to the high porosity, successive dilute polysilazane coatings and firing steps could be used to increase the density of these structures.

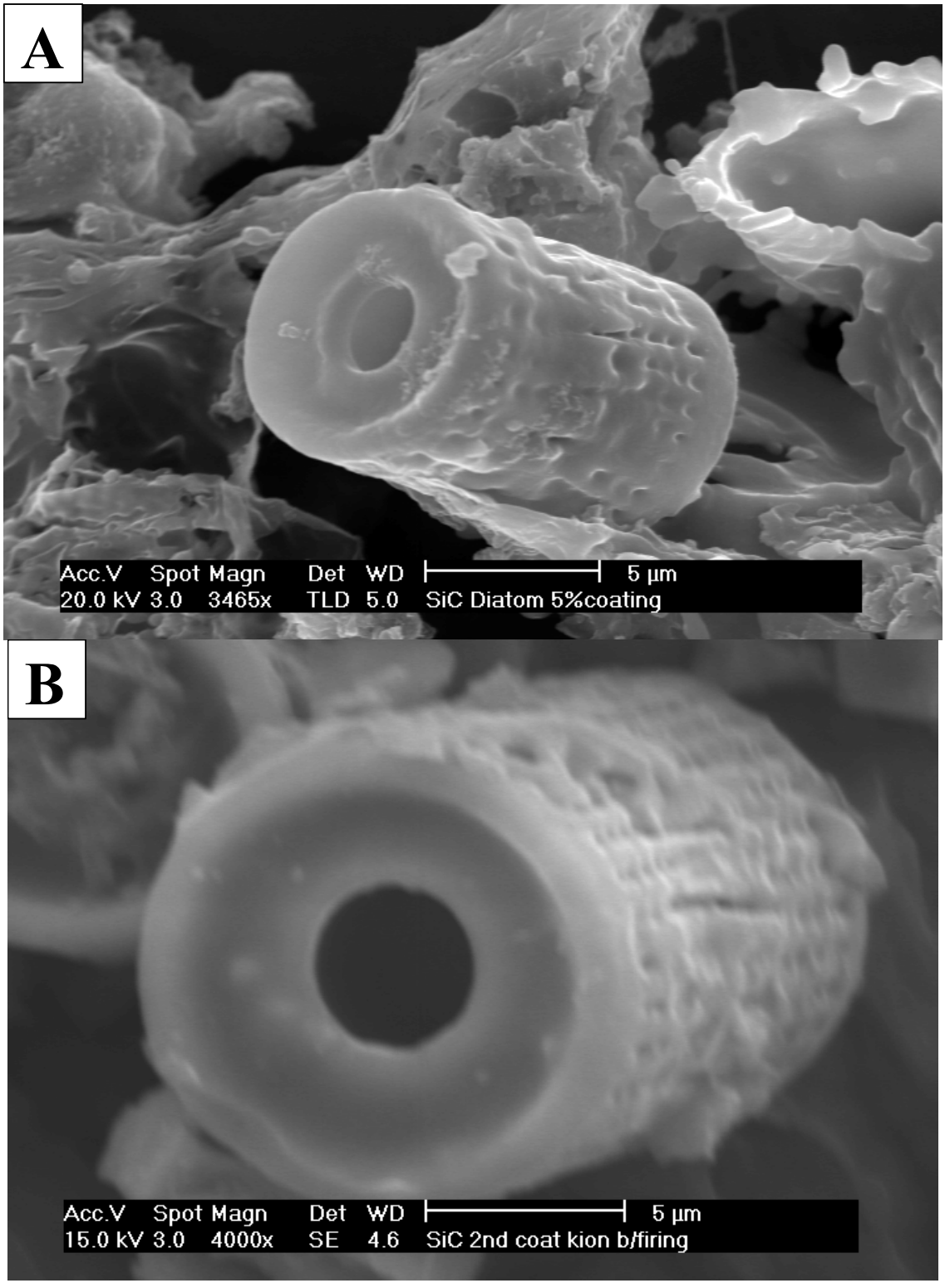

Figure 4-2 SEM Images of Polysilazane Coated Diatoms

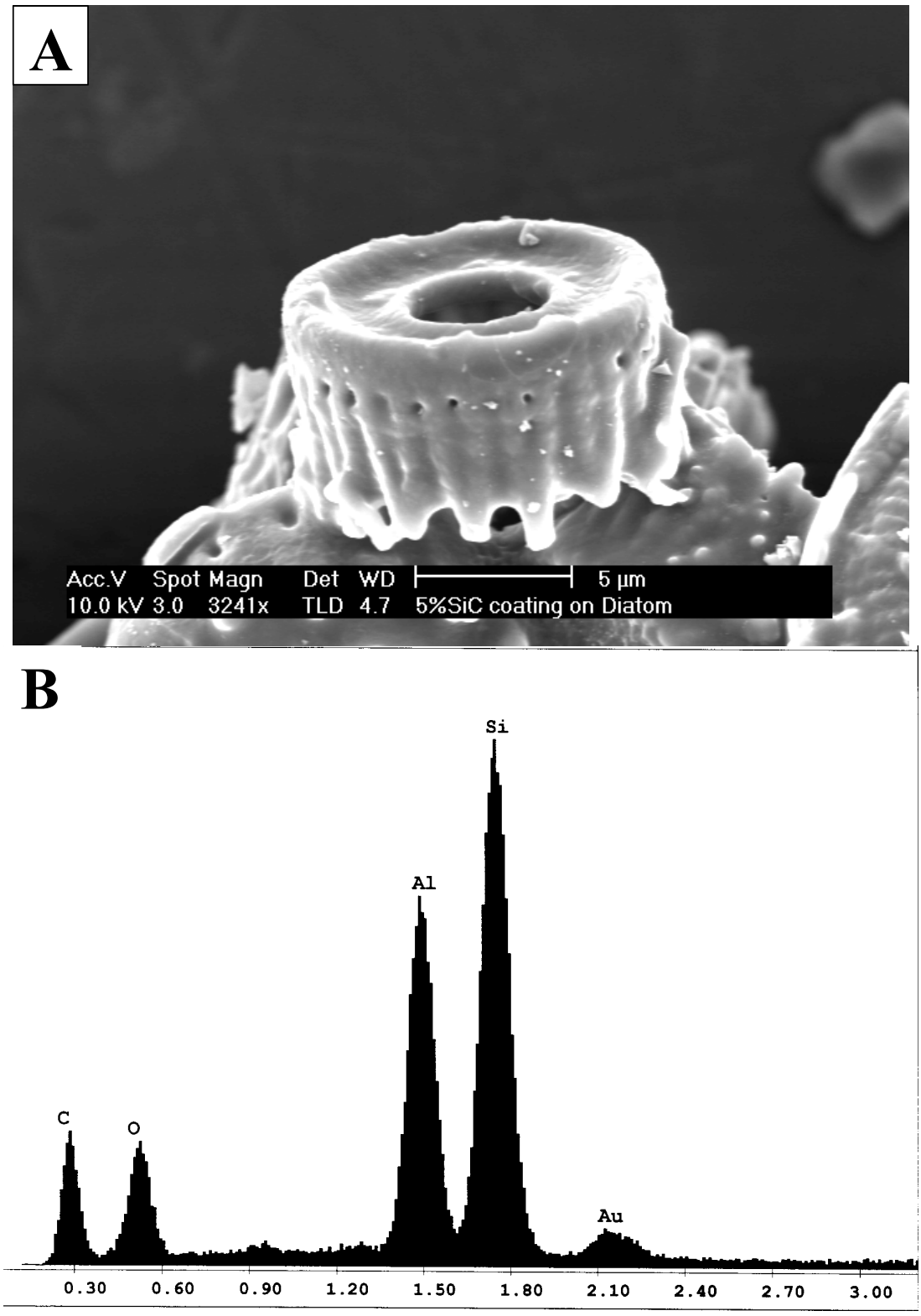

Figure 4-3 EDS and SEM Analysis of SiC Coated Diatoms

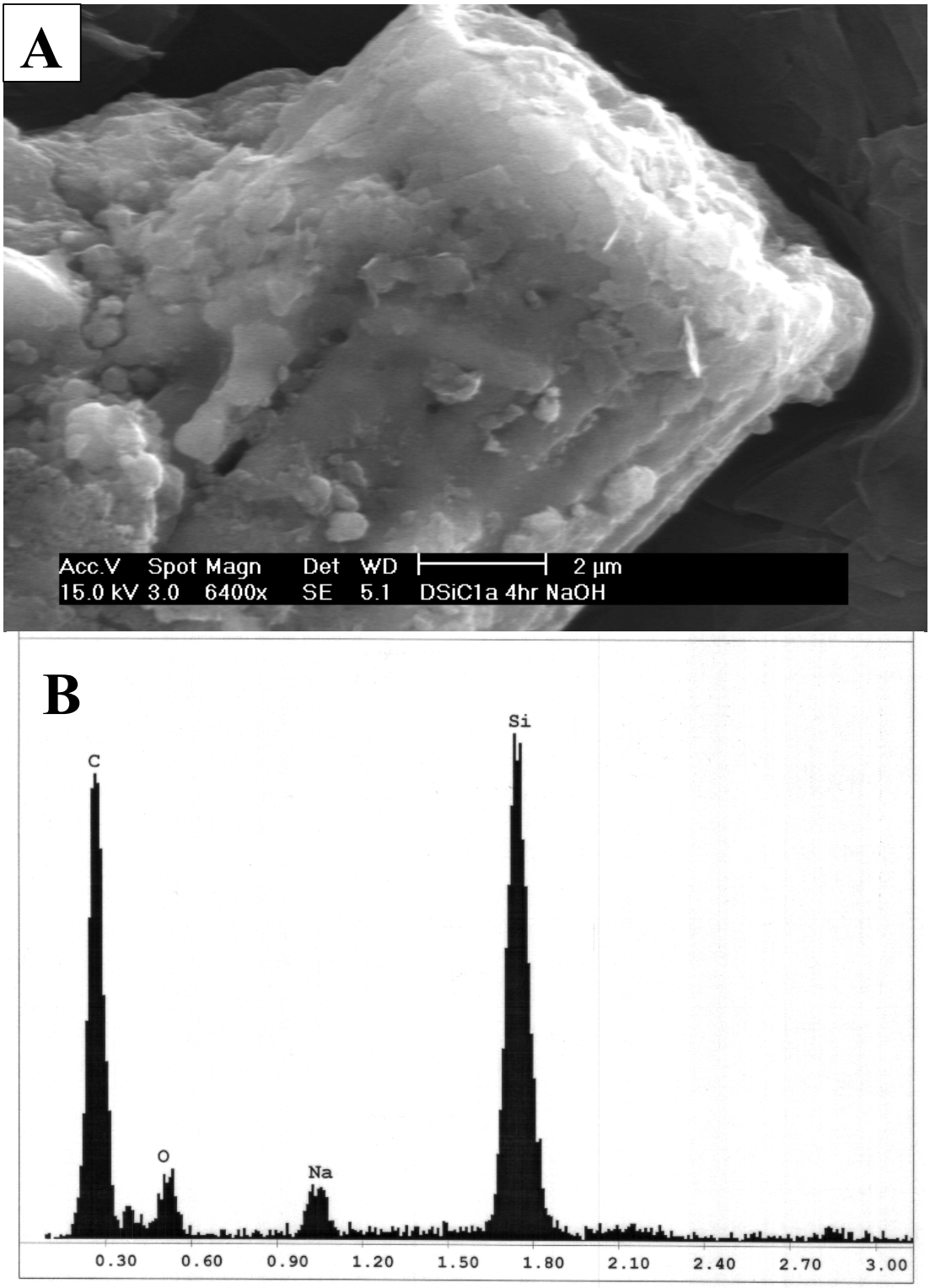

Figure 4-4 SEM and EDS Analysis After NaOH Treatment

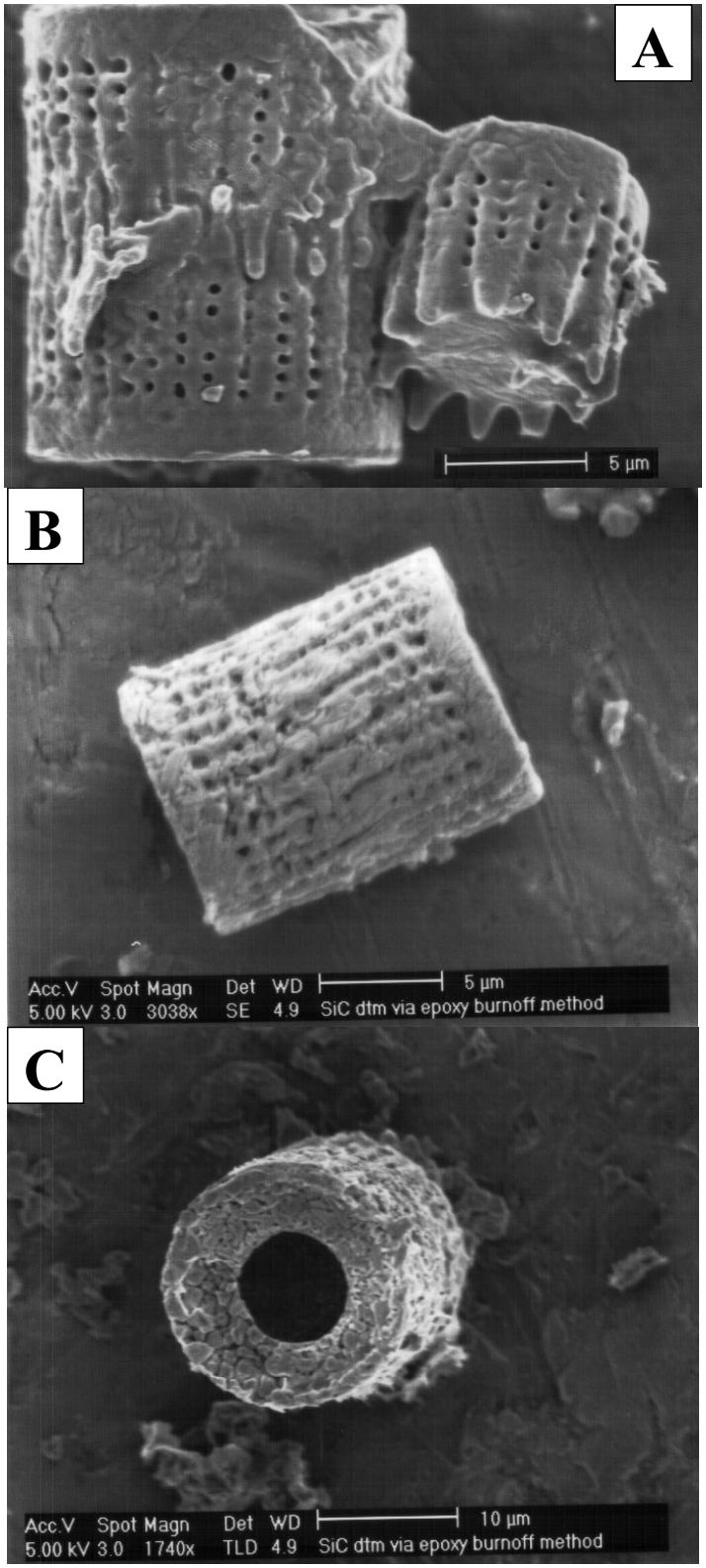

Figure 4-5 Images of Piolysilazane Coated Epoxy Frustules Pre and Post Firing

Chapter 5

Titania Gas Sensor Fabrication and Testing

Titania is a commonly used semiconductor for gas sensing[61]. Titania sensors are typically used as potentiometric sensors, i.e. the resistance changes as a function of gas concentration. When oxygen is absorbed onto the surface of the titania at an operating temperature of 300-500ºC, oxygen diffuses into the crystal. As each oxygen atom is incorporated into the crystal, it is ionized, creating a O^{2-} ion. This process consumes free electrons from the crystal surface, leaving a positively charged space charge on the crystal surface. At the grain boundaries a schottky barrier is present, which inhibits charge carrier movement. The presence of reducing gasses lowers the schottky barrier, which causes a conductivity increase proportional to the gas concentration. The important criteria in evaluating gas sensor performance are the magnitude of the conductivity change, the rate of response, relaxation time, consistent baseline, and repeatable response. The gas sensor was made from a single Titania converted frustule (Figure 5-1A). The Titania frustules were synthesized by exposing silica frustules to TiF_4 gas at 350ºc for 4 hours, which resulted in the formation of $TiOF_{2(s)}$ according to a reaction of type:

$$TiF_{4(g)} + \frac{1}{2} SiO_{2(s)} \rightarrow TiOF_{2(s)} + \frac{1}{2} SiF_{4(g)} \qquad (1)$$

Heating the product of the prior reaction in air at 400ºC for an additional 4 hours resulted in the formation of TiO_2, by the reaction:

$$TiOF_{2(s)} + \frac{1}{2} O_{2(g)} \rightarrow TiO_{2(s)} + F_{2(g)} \qquad (2)$$

An SEM image of the titania sensor is shown in Figure 5-5B. X-ray diffraction showed that the structure is the anatase polymorph of TiO_2 (Figure 5-6A), and transmission electron microscopy showed the grain size to be < 100nm (Figure 5-6B). Secondary electron images were taken that show the frustule structure was preserved through the reaction. In order to measure the resistance of the titania diatom in response to changes in ethanol gas concentrations, ohmic contacts were made with the frustule by attatching it to a platinum grid of interlocking 2μ wide contacts spaced 1μ apart on a silicon substrate. A single titania converted frustule was harvested from a previous SEM specimen by welding a tungsten micromanipulator needle to the diatom via focused platinum deposition in a FIB (FEI Dual-Beam DB-235 Focused Ion Beam and Scanning Electron Microscope), and then lifting it off the aluminum substrate. Figure 5-1B shows the tip of the tungsten needle micromanipulator in contact with the titania frustule prior to attachment via platinum deposition. Figure 5-2A shows the Titania frustule welded to the micromanipulator tip after having been lifted off the substrate. The frustule was then placed onto the contact grid using the in-situ micromanipulator (Figure 5-3). The weld was then milled away to separate the frustule and needle. Samples #1 and #2, shown in Figure 5-4A, were made by welding the frustule to the grid using FIB platinum deposition. Platinum deposition was inaccurate due to a system malfunction and caused the circuit to be shorted. Ion milling was performed such that only a single positive and negative interconnect were connected to the sample, removing the short circuit. The finished sensor#1 can be seen in Figure 5-4B after a cleaning milling step was performed to expose the titania frustule surface, and further reduce the possibility of a short circuit. Sample #3 was made by simply

placing the frutule across the grid using the micromanipulator. The diatoms in each case were gently pressed onto the grid using the micromanipulator tip.

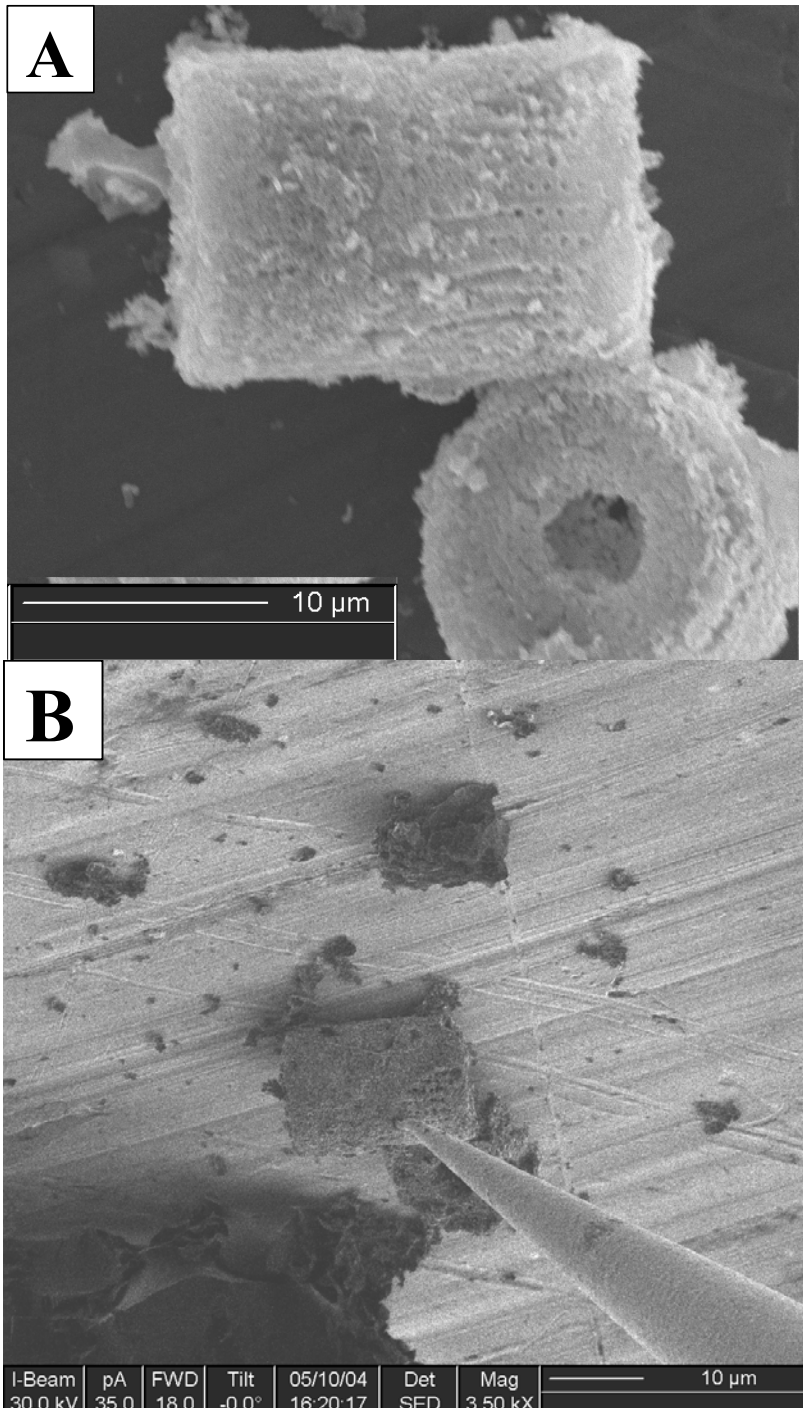

Fig 5-1 SEM Images of Micromanipulator Attachment to Diatom

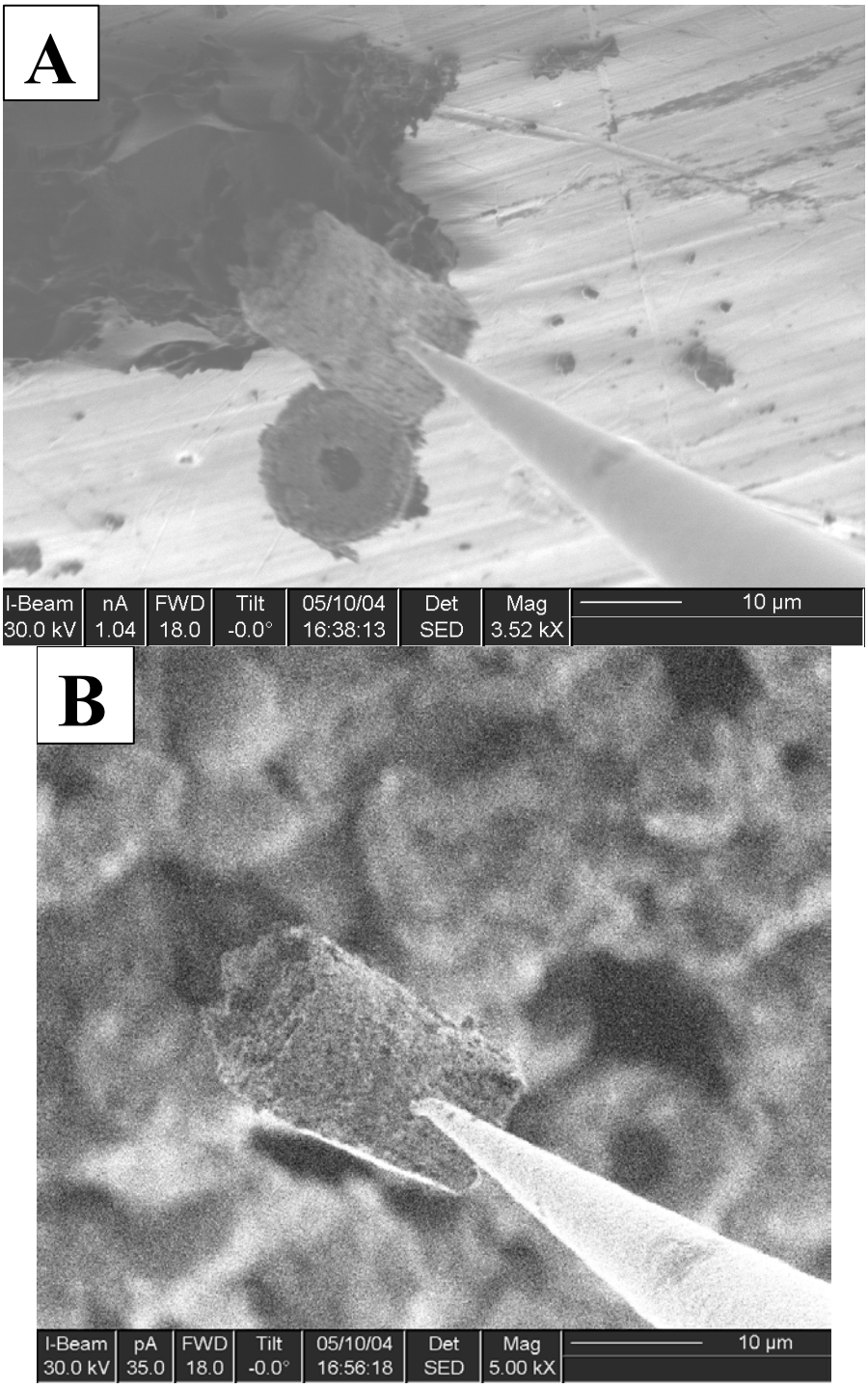

Fig 5-2 Attached TiO_2 Diatom Lifted Off the Substrate

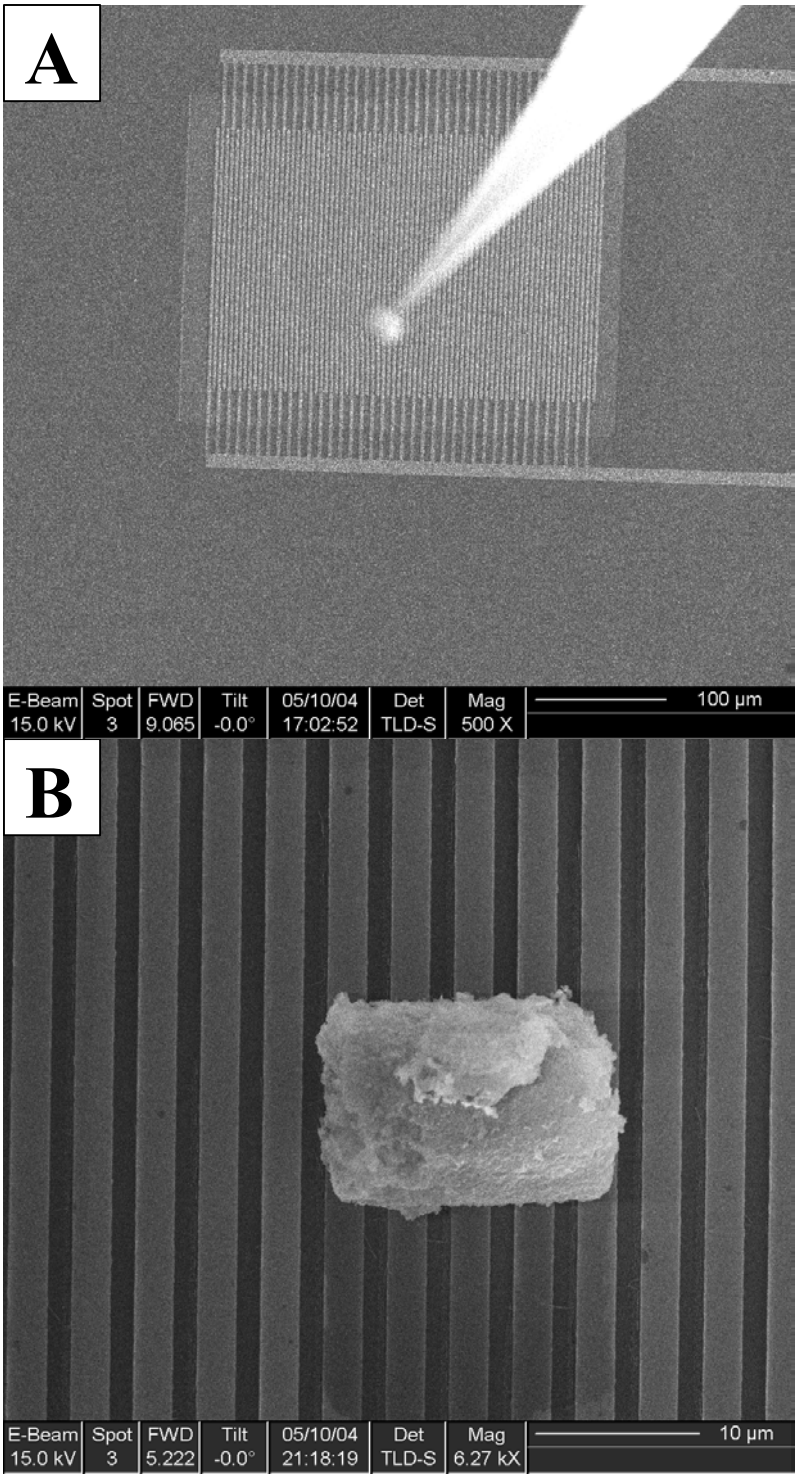

Figure 5-3 TiO_2 Diatom Positioned on the Contact Grid

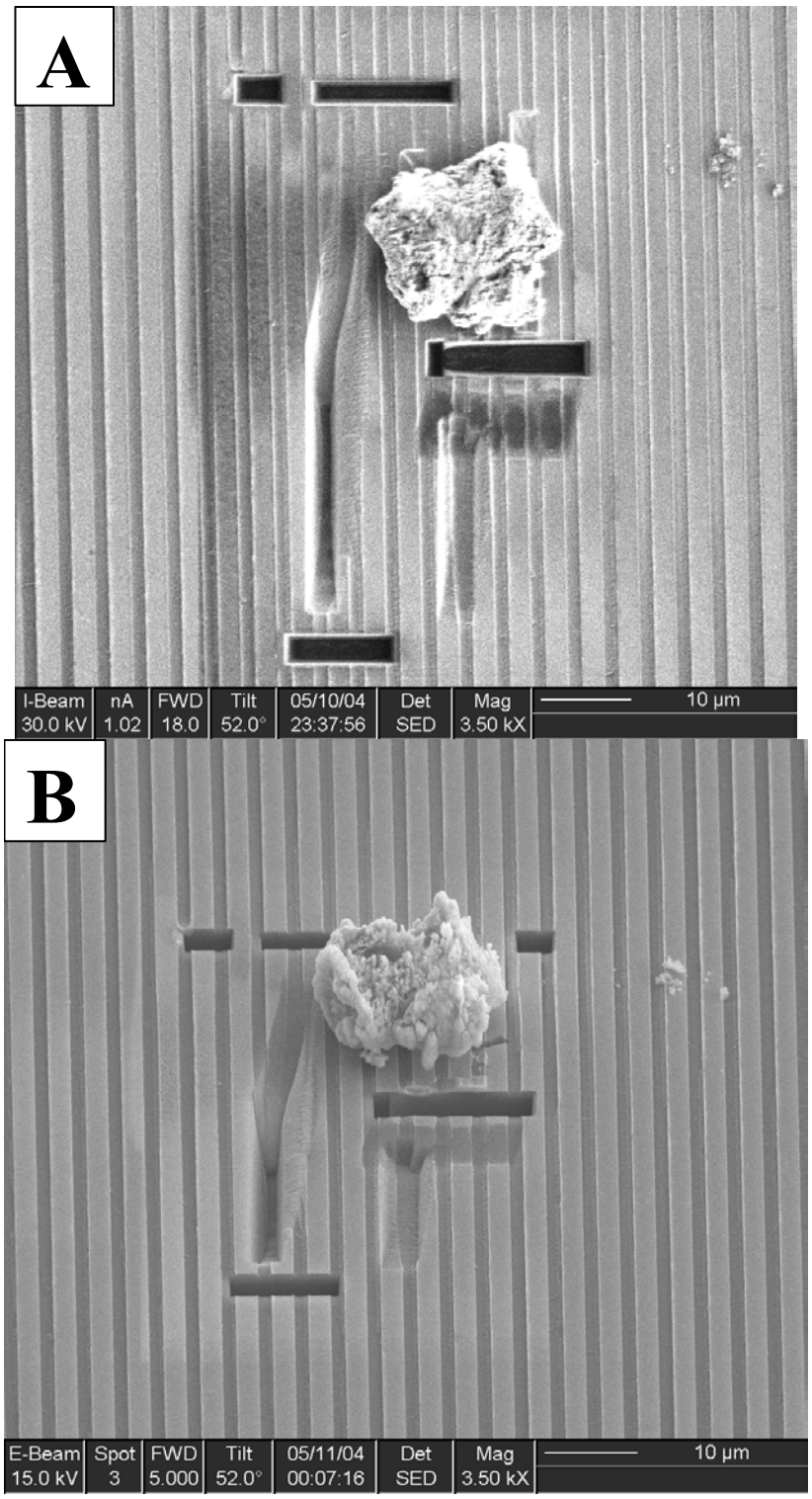

Figure 5-4 SEM Images of Sensor#1

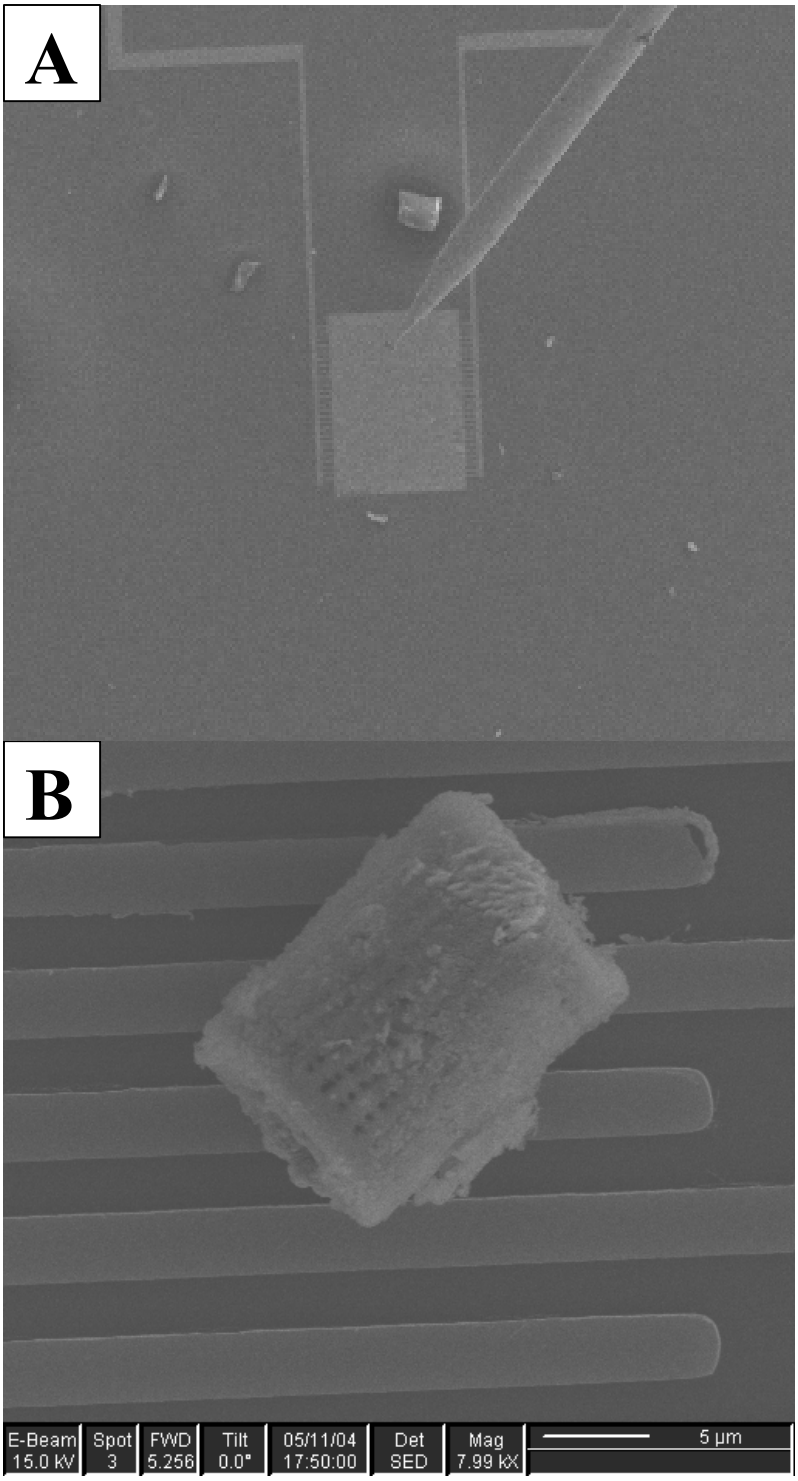

Figure 5-5 SEM Images of Sensor #3

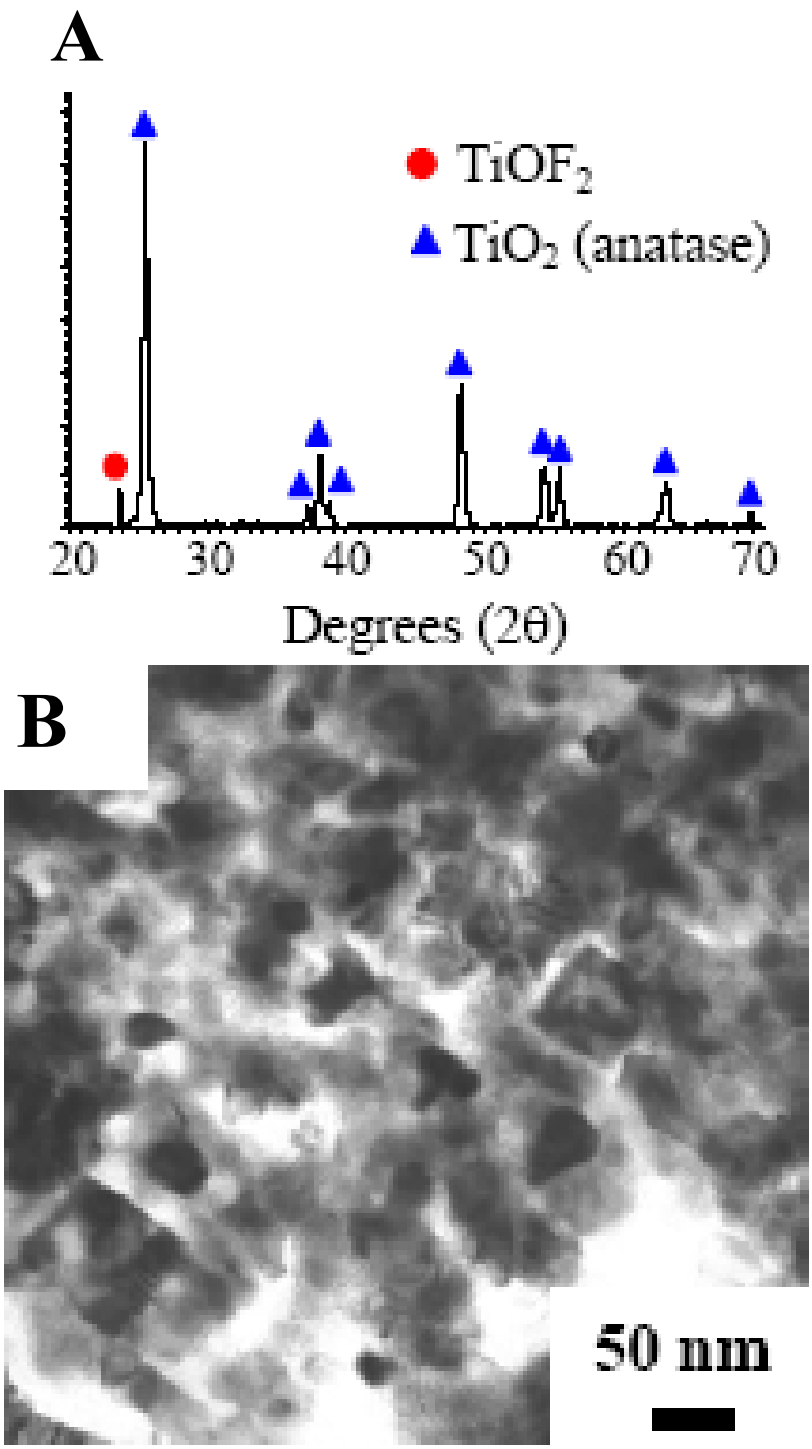

Figure 5-6 TEM Analysis of the Titania Sensor Frustules

The three sensors each based on a single TiO_2 diatom were exposed to different levels of ethanol and hydrogen vapor at several temperatures. Conductance measurements were performed at a constant gas flow rate of 100 sccm. Current flowing through the TiO_2 diatom sensor was recorded as a function of time at a constant voltage of 100 mV. The dynamic electrical response was plotted as a function of time. Since TiO_2 is an n-type semiconductor, the current passing through the sensor increased as expected upon ethanol and hydrogen exposure.

Upon testing it was found that Sample #2 had relatively high conductance and did not respond at all to the gasses. This indicated that the circuit was shorted. Samples #1 and #3 did respond to the gasses and the dynamic response to various conditions is shown in the following figures. Sample #1 was tested using both hydrogen and ethanol vapor. In the case of the hydrogen test, three concentrations were used: 400ppm, 800ppm, and 1600ppm. The tests were conducted at a constant temperature of 300ºC. Figure 5-7 shows the response of sensor #1 to hydrogen. The change in resistance was slow and did not show any constant trend of consequence. Exposure to each concentration caused a decrease in resistance. However, the resistance change was inconsistent and the baseline resistance wandered badly. The baseline resistance steadily decreased, which may indicate a surface interaction with the hydrogen gas that was non-reversible under these conditions.

Figure 5-8 shows the response of sensor #1 to a single concentration of ethanol (7.8%) at 300ºC. Response time is fast and the baseline resistance as well as response magnitude are consistent as a function of time. The recovery time is relatively slow. The

sensor takes over 10 minutes to return the baseline resistance after the atmosphere was changed from air + 7.8% ethanol vapor back to air. Figure 5-9 shows the response of sensor #1 to several relatively high ethanol concentrations. The sensor response appears to be saturated as the magnitude of the response is very small when the concentration is switched from 1.95% to 3.9% and from 3.9% to 7.8%. Recovery time is extremely slow, and the baseline consistency cannot be evaluated, as the sensor recovery time never comes close to reaching the original baseline.

Figure 5-10 shows the response of sensor #3 to ethanol at concentrations of 300ppm and 1000ppm. The responses to the two 300ppm pulses were nearly identical. The 300ppm responses were characterized by a sharp transient peak, which quickly settled to a steady-state value. The magnitude of the sharp transient peak was approximately 3 times larger than the steady state value. The cause of this transient response is unknown. It can readily be seen that the response and recovery time are significantly faster than previously seen in sample #1. The ethanol concentrations were much greater in the tests performed on sample #1 so a direct comparison cannot be made.

There are however, several possible explanations that could explain this behaviour. Sample #1 was connected to the grid via platinum deposition. A small amount of platinum was inadvertently deposited onto the outer surface of the diatom. An attempt was made to clean the diatom surface by ion milling the platinum away. Unfortunately, the FIB was not equipped with an Energy Dispersive X-ray detection system, so a means of determining the cleanliness of the anatase frustule surface was unavailable. If platinum was contaminating the anatase- gas interface, the interaction area would be reduced relative to sample #3. The smaller gas-solid interaction area could

be responsible for lengthening the response time. Alternatively, the longer response and recovery times seen in sample #1 could be caused solely by the much higher ethanol concentrations used. As ethanol is introduced to the system, it adsorbs onto the frustule surface and interacts with the surface. As the ethanol gas concentration increases the ethanol surface coverage increases until eventually a monolayer is formed. It may be that as the surface coverage nears this point the relative response magnitude decreases. After the monolayer is formed absorption of ethanol into the frustule may continue lowering the resistance. The longer response time may be related to the diffusion of ethanol to the grain boundaries inside the frustule. At high concentrations a layer of ethanol would be expected to build up on the surface.

The much longer recovery time seen in the Sample #1 tests may be related to the time needed for the thick ethanol layer to dissipate. It is also certainly possible that a combination of the platinum effect and the concentration effect were responsible for the observed difference in response and recovery time. Further experiments would need to be conducted in which both samples are tested under the same conditions to determine whether the platinum deposition is influencing the measurement.

Figure 5-11 shows the response of sensor #3 to ethanol concentrations of 500ppm, 1000ppm, and 2000ppm at 300ºC. The relative magnitudes of the response to 500ppm, 1000ppm and 2000ppm were very non-linear. The 500ppm response showed a transient spike very similar to the behaviour seen in the previous 300ppm test. The magnitude of the 1000ppm response was much larger than double the 500ppm response, while the 2000ppm response was significantly less than double the magnitude of the 1000ppm response. The response and recovery time were both reasonably fast, though the

recovery time of the 2000ppm response was significantly longer than the 1000ppm and 500ppm response. The 2000ppm response was also somewhat inconsistent. The steady state value and recovery were both jagged. Figure 5-12 shows the response of sensor #3 to ethanol concentrations of 500ppm, 1000ppm, and 2000ppm at 400ºC. Under these conditions the sensor performance was exceptional. Since the response time and recovery were extremely fast and the relative response magnitude seemed to follow power law behavior, the results under these conditions were analyzed quantitatively. Figure 5-13 shows the same results as Figure 5-12 with data points added, where each point corresponds to one second of measurement. When ethanol vapor was introduced, the signal changed abruptly and quickly reached a plateau. For 500ppm ethanol, the sensitivity or relative change in conductance $\Delta G/G_0$ is 2.4 times, where ΔG and G_0 are the change in conductance caused by ethanol and the conductance in air. The value increased to 3.4 and 6.3 as ethanol concentration increased to 1000 and 2000ppm as shown in the insert of Fig. 5-13. The response times (defined as the time to reach 80% full response change) for 500, 1000, and 2000 ppm ethanol vapor at 400°C are 48, 18, and 14 seconds respectively. Most amazingly, the TiO2 diatom sensor recovered fully in approximately one second after switching back to air. Figure 5-14 clearly shows the speed of the sensor recovery for the 1000ppm ethanol concentration. For TiO2 sensors, 100s response, 1500 ~ 2500s recovery time in 1200ppm ethanol has been reported[68]. In another article, a TiO2 ethanol sensor took 2 min to reach 90% full response, and took 1 min to obtain 30% recovered after switching back to air.

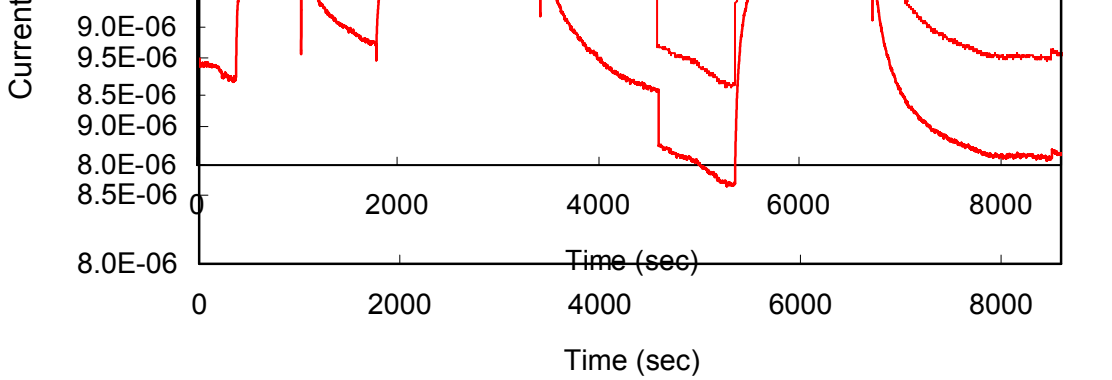

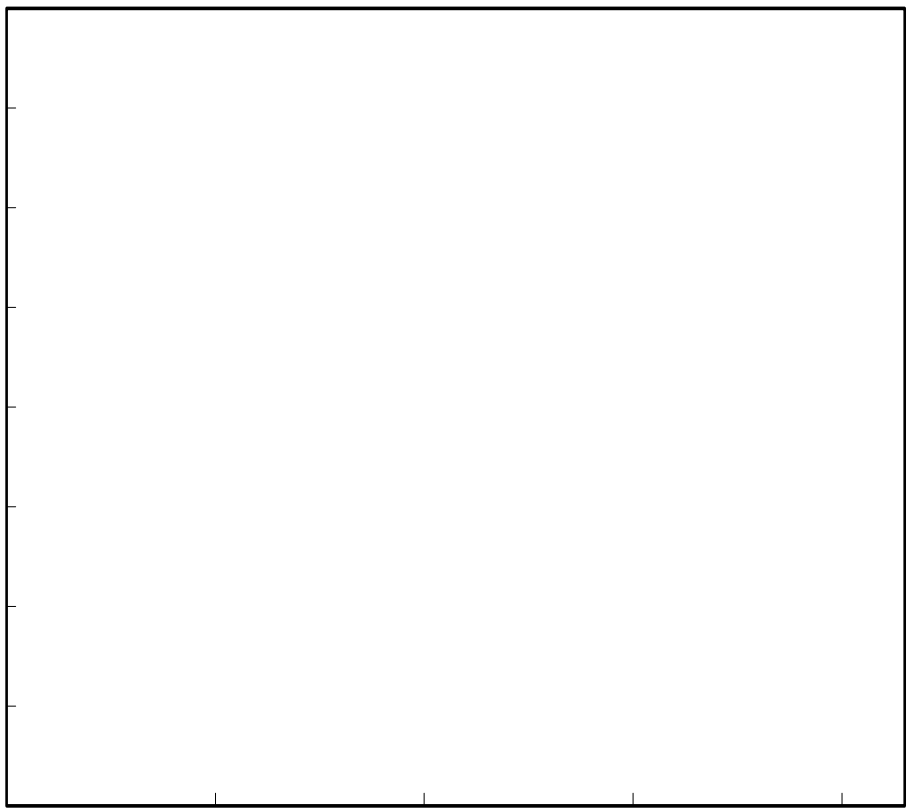

Figure 5-7 Electrical response of sensor #1 to Hydrogen

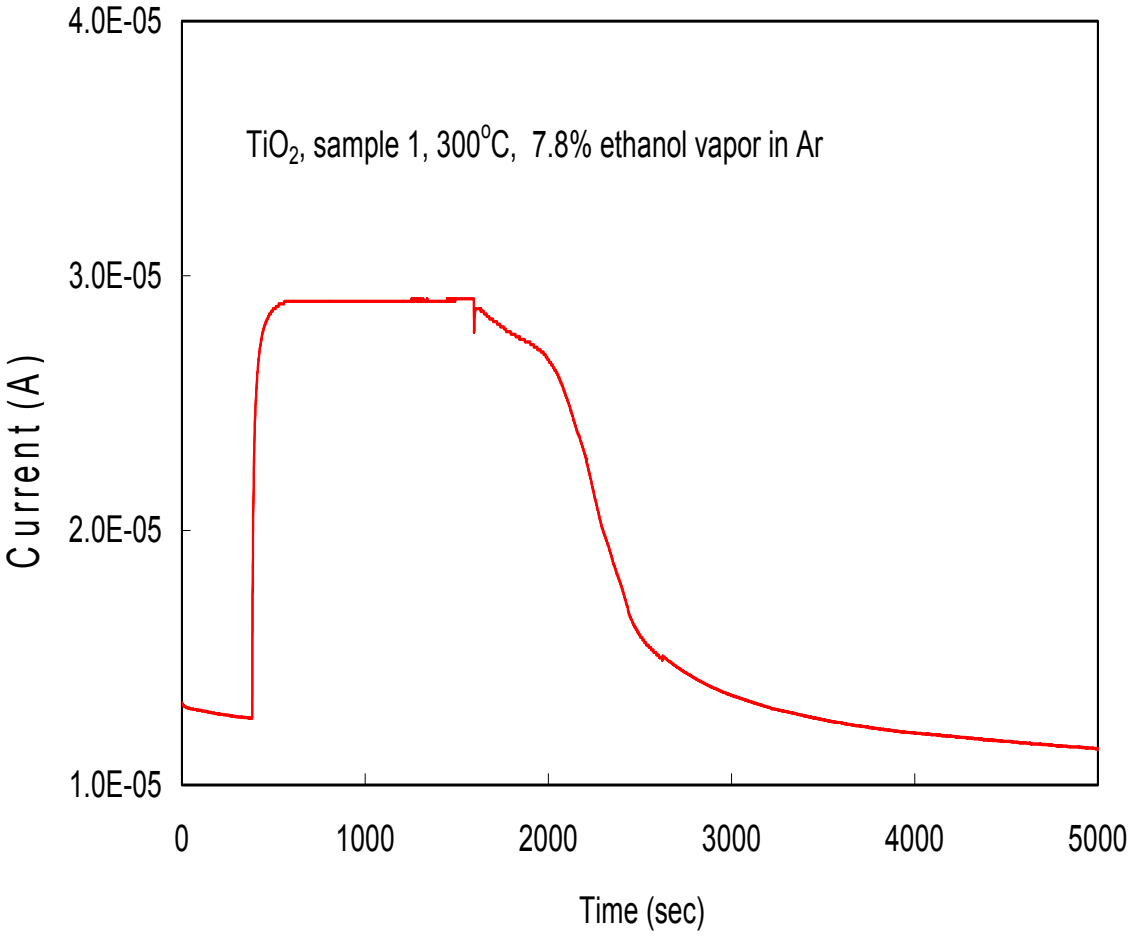

Figure 5-8 Response sensor#1 to 7.8% Ethanol at 300°C

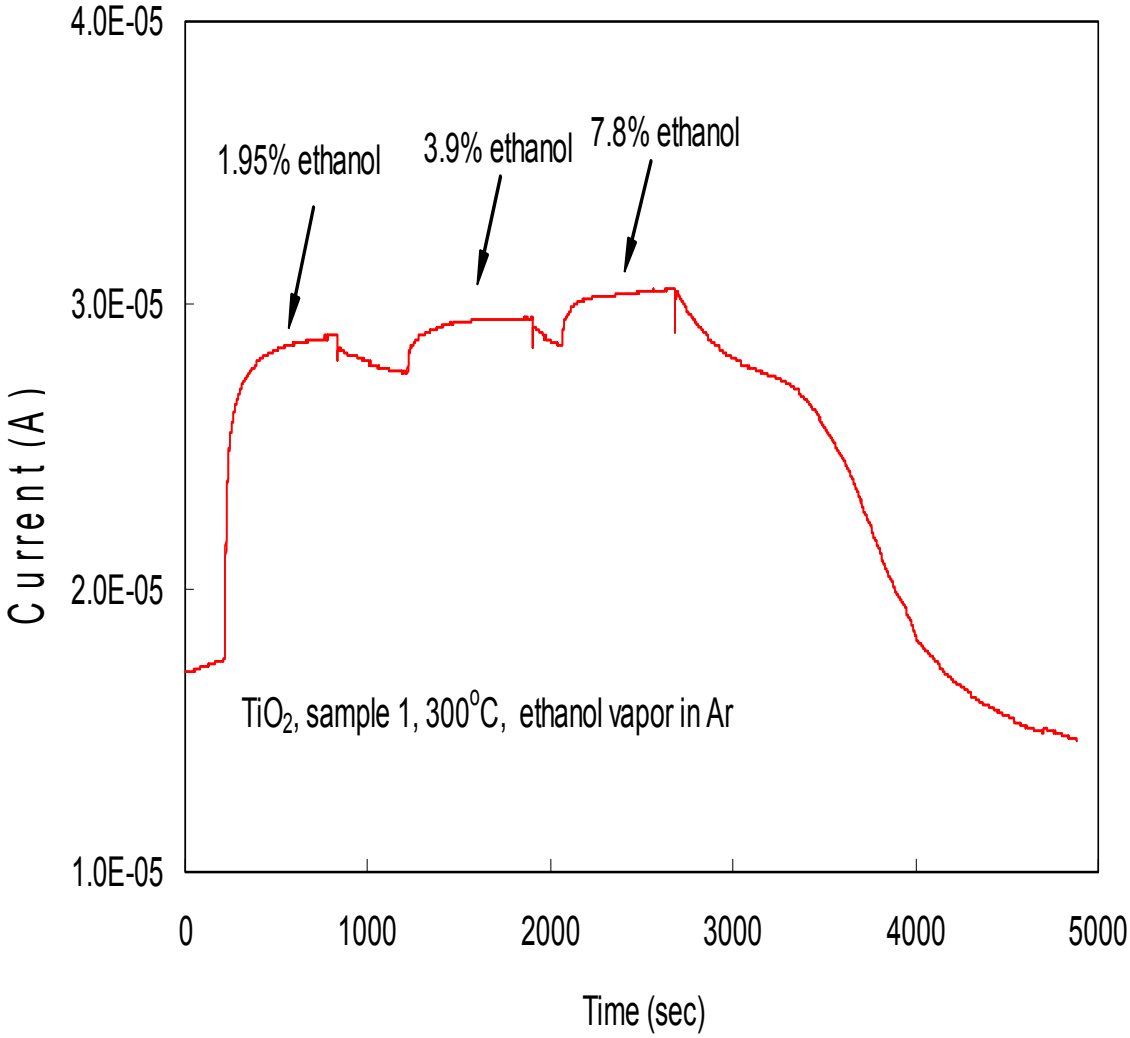

Figure 5-9 Response of sensor #1 to 1.95%, 3.9%, 7.8% Ethanol at 300°C

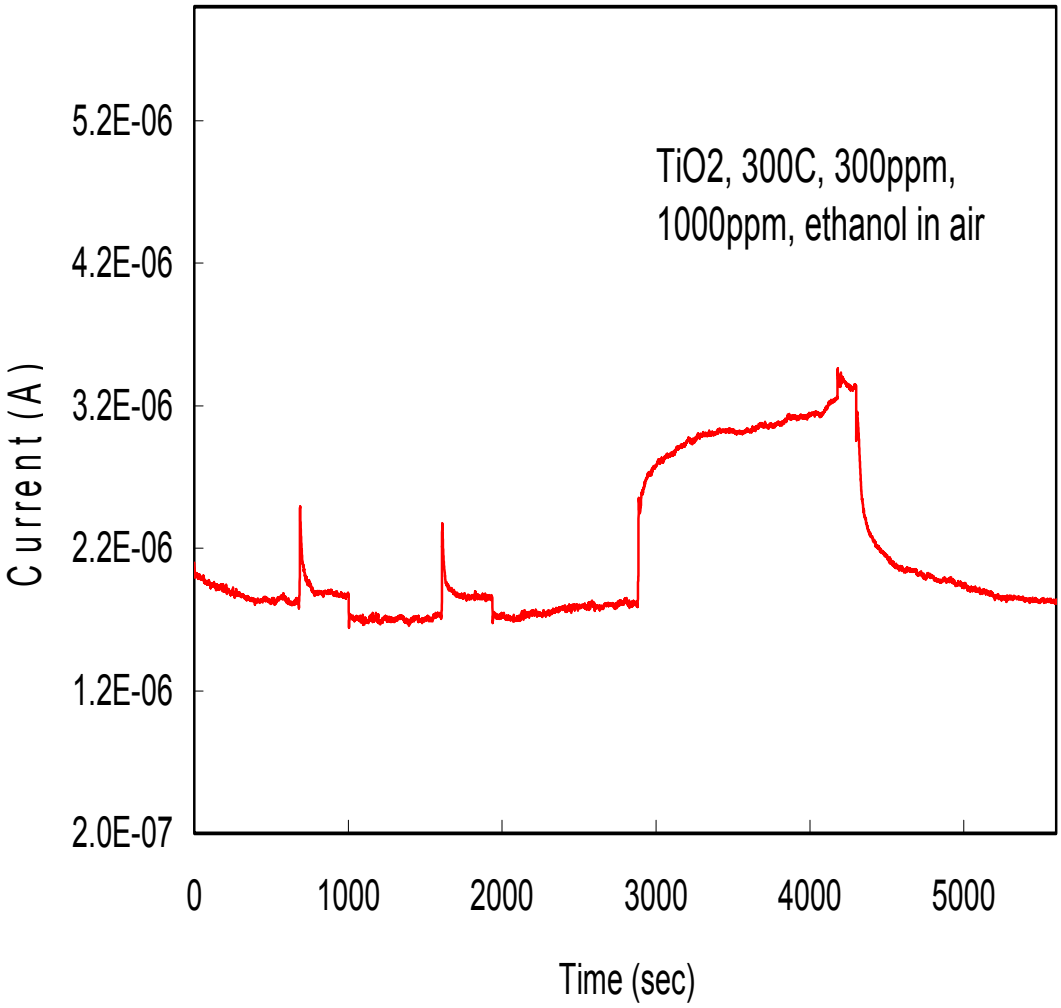

Figure 5-10 Response of Sensor #3 to 300ppm and 1000ppm Ethanol

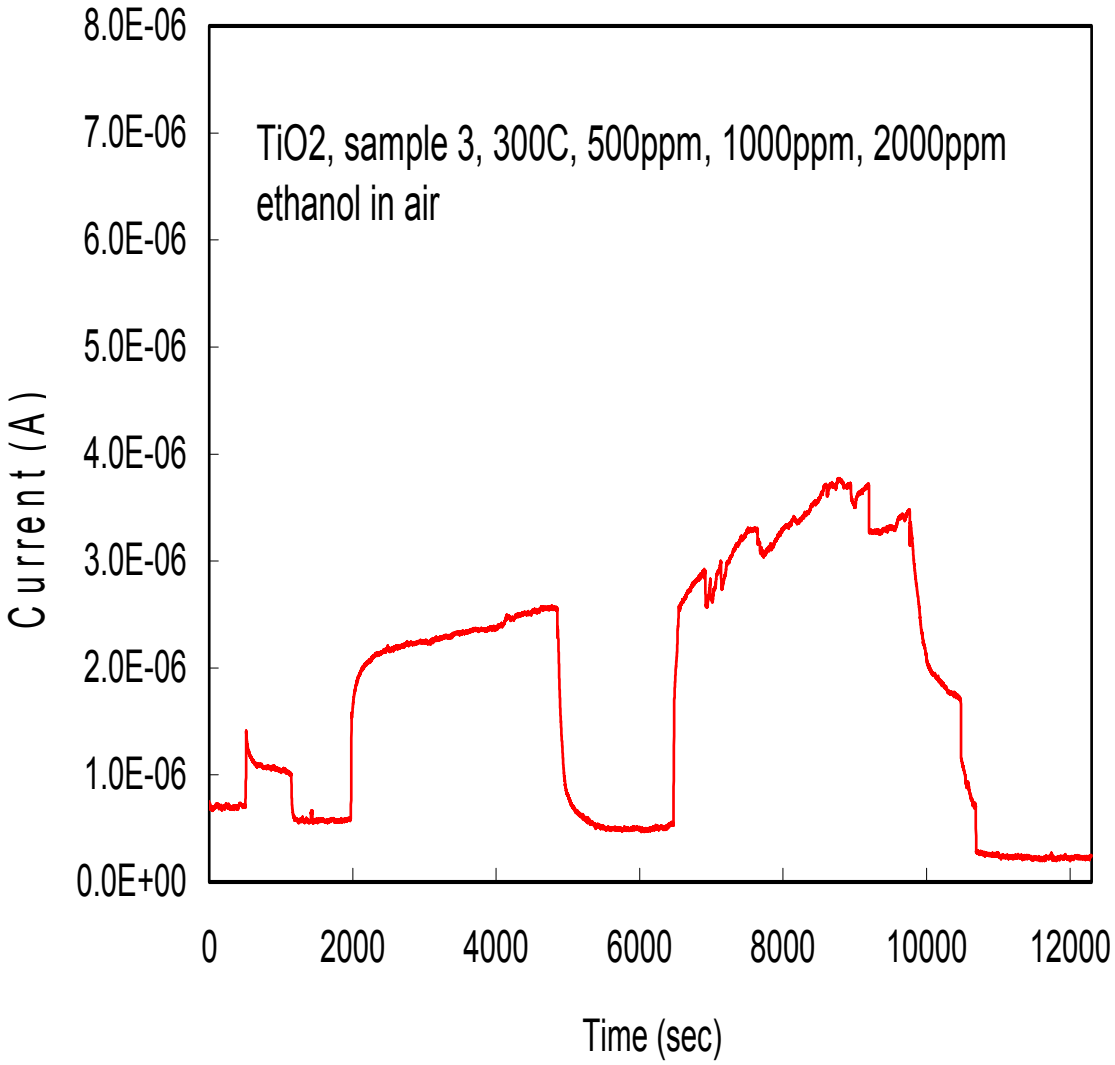

Figure 5-11 Response of Sensor #3 to 500ppm, 1000ppm, and 2000ppm ethanol

It is clearly evident from the insert in Fig. 5-13 that the dependence of sensitivity on ethanol concentration follows the well-know power law behavior $\Delta G/G0 = A[gas]B$. The constant B denoted by the log-log plot slope equals to 0.84, indicating surface interaction with pre-adsorbed oxygen ions rather than bulk diffusion of oxygen vacancies dominates ethanol-detecting process. Figure 5-14 shows the electrical response of the TiO2 sensor is correlated with structural features. As shown in the SEM (Fig. 5-1a) and TEM (Fig. 5-6b) micrographs, TiO_2 diatom consists of nano-sized grains less than 100 nm with nanopores between the grains. The surface to volume ratio is extremely high. As grain size or film thickness is smaller than or in the same order of magnitude as the Debye λ_D, depletion zone could extend through the entire grain[61-62]. However, considering the 5 μm entire diameter of the TiO_2 diatom sensor, the 1-second full recovery time suggested other mechanisms might play important roles. More work is needed to elucidate the underlying mechanism responsible for the superior response and recovery behaviour of this sensor. Sensitivity, response time and detecting limit could be significant improved by doping TiO_2 with other elements such as Cr, Cu, Nb, Sn, W, Sr, Ce, Y and Tb.

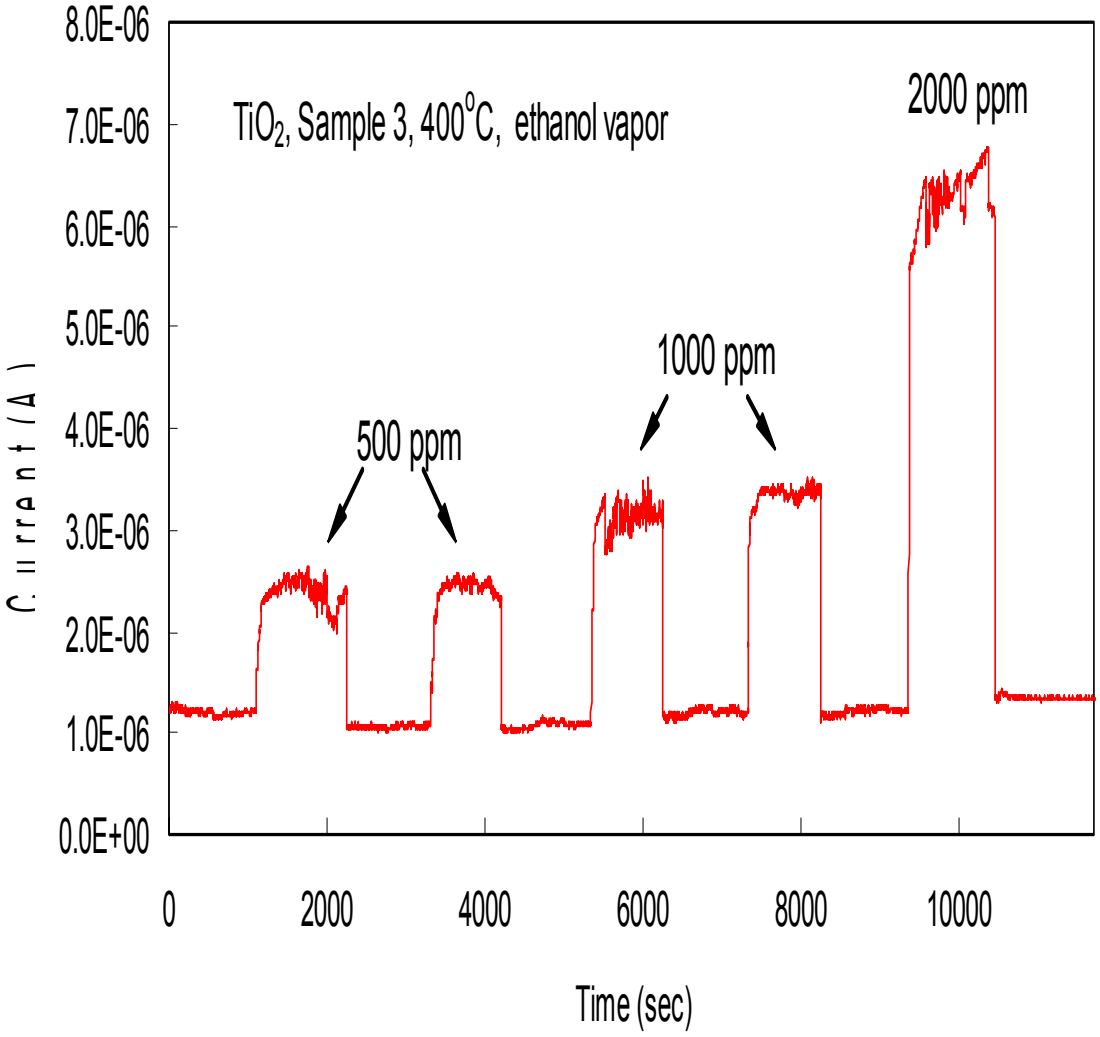

Figure 5-12 Response of sensor #3 to 500ppm, 1000ppm, and 2000ppm ethanol at 400C

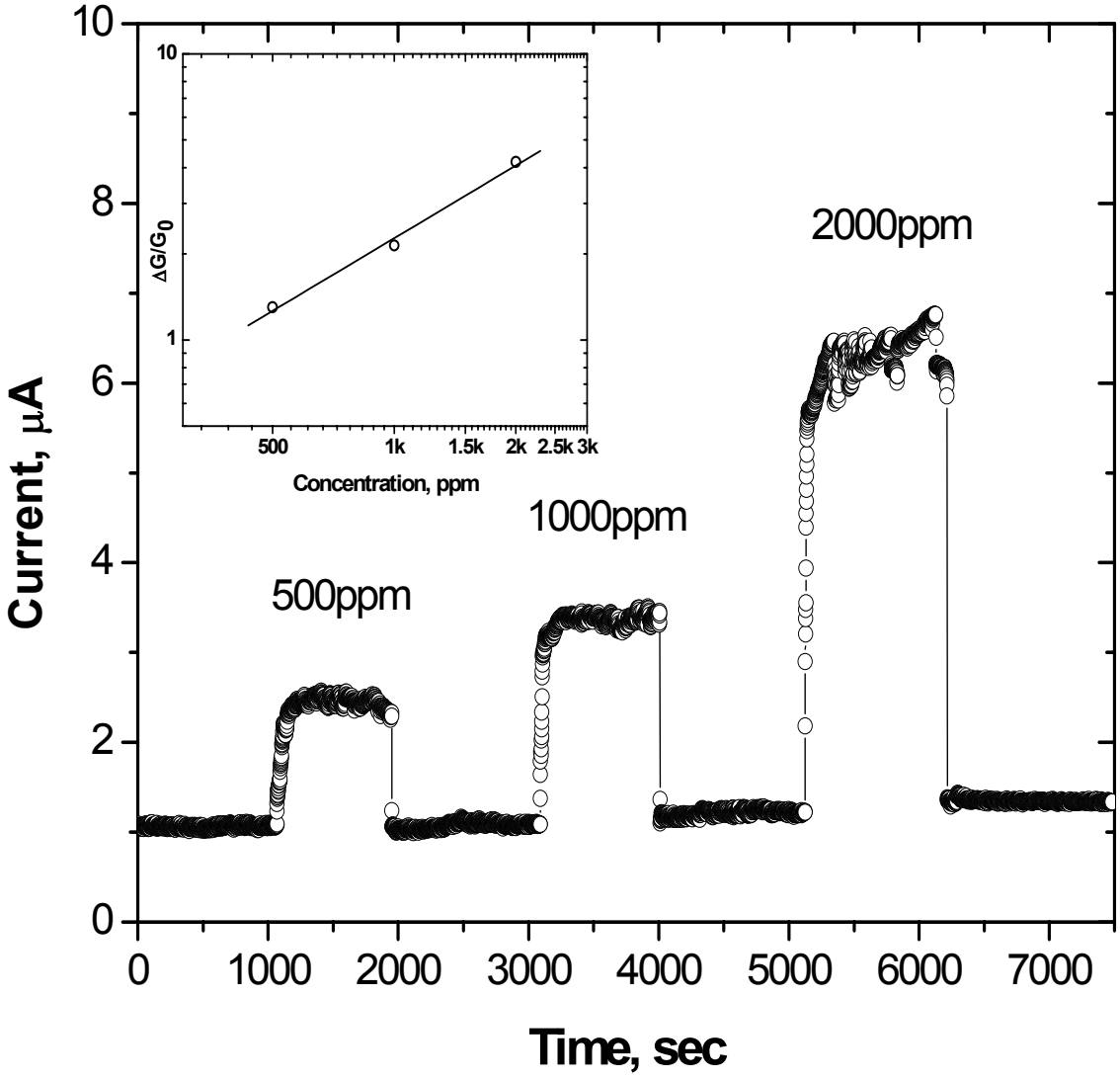

Figure 5-13 Data used to obtain the power law response plot

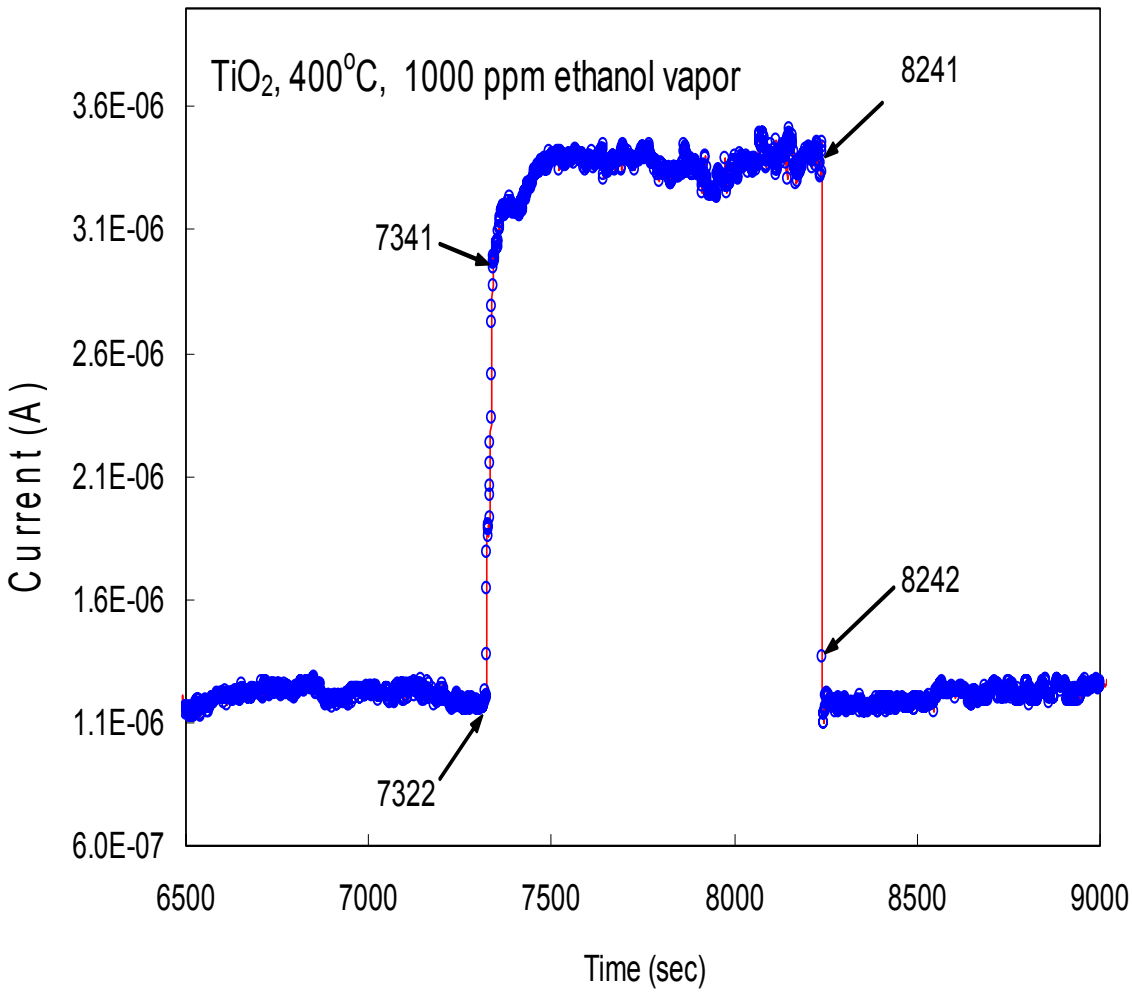

Figure 5-14 Fastest response and recovery reported for this sensor type

Chapter 6

Barium Titanate Frustules via Low Temperature Hydrothermal Reaction

Barium titanate has useful ferroelectric properties, which when coupled with the complex, 3-dimensional high surface area geometries of diatom frustules, could potentially be used as the basis of a variety of devices. Microactuators, capacitors, sensors, or optical devices are possible due to the piezoelectricity, high dielectric constant and high index of refraction that barium titanate possesses[85]. It has been reported in the literature that titania can be reacted with barium hydroxide to form barium titanate under hydrothermal conditions. [82-84] The present work demonstrates that barium titanate can be synthesized in a shape preserving reaction to convert silica diatom frustules into barium titanate. This is accomplished by reacting barium hydroxide hexahydrate with titania frustules[86]. Titania diatom frustules have previously been synthesized using a halide gas-solid displacement reaction in which titanium tetrafluouride reacts with silica to form titania frustules and silicon tetrafluouride gas. Titania will react with barium hydroxide hexahydrate under hydrothermal conditions according to the following reaction.

$$2TiO_2 + 2Ba(OH)_2 *(H_2O)_8 \Rightarrow 2BaTiO_3 + 10H_2O$$

The reaction was conducted in a sealed stainless steel tube in the presence of water vapor. The thermal treatments were very modest, ranging from 125°C to 225°C. However, sufficient DI water was added to the reaction vessel to raise the pressure to 100atm for each experiment. Initial experiments were conducted in which a 1-2 molar ratio of TiO2 frustules and Barium Hydroxide Hexahydrate were added to a steel tube,

along with sufficient DI water to raise the pressure to 100atm, and welded shut. The Tube was heated at a rate of 5°C/min to temperatures of 150°C and 225°C for 6 hours. Following the thermal treatment, the tubes were cut open to extract the samples. SEM analysis of the samples heat treated at 150°C and 225°C is shown in Figures 6-1 and 6-2. The shape preservation in the 150°C sample was quite good. The overall shape of the aulacasiera-derived frustule was retained, as well as the pore structure. It appears that the porosity of the sample increased as well. The shape preservation of the 225°C sample was much worse than the 150°C sample. Although the general shape of the frustules can be seen after reaction, the fine features are gone, and material appears to have been deposited on the sample. XRD was also conducted on each sample. The patterns were nearly identical, and a representative pattern is shown in Figure 6-3. This diffraction pattern shows that barium titanate was formed. However, a large amount of barium carbonate was also formed. Barium carbonate could not have been formed by this reaction, as there was no source of carbon in the precursors used. At least there shouldn't have been any source of carbon. Barium Hydroxide however will react with the carbon dioxide in air to form barium carbonate. X-ray diffraction was done on the "BaOH*8H2O" precursor. The results are shown in Figure 6-4. Barium carbonate is clearly a major component of the "barium hydroxide." This indicates that the hydrothermal reactions were successful since barium titanate and the already present barium carbonate were the major phases identified by diffraction. It was not clear, however whether barium carbonate was incorporated in the frustules, or as discrete impurity particles. Electron dispersive spectroscopy was done on several frustules to

determine the elements present. A carbon peak would be consistent with barium carbonate being incorporated in the frustule walls.

Figure 6-5 shows an EDS pattern from a frustule wall. Barium, titanium, oxygen, and carbon were found to be present. This shows that barium carbonate was present in the frustules. In order to form phase pure barium titanate, a new barium hydroxide precursor was obtained and opened in inert atmosphere. New stainless steel reaction vessels were also obtained with threaded compression fittings and much higher wall thickness to allow for higher pressure experiments in the future. Since the previous experiments used a 2-1 molar ratio of barium hydroxide to titania, and the Titania to barium titanate reaction appears to have gone to completion, despite the barium hydroxide having been partially converted to barium carbonate, the ratio was reduced to 1:1 stochiometric.

Based on the results of the previous experiments in which it was shown that frustule feature preservation was better at lower temperature, the next experiment was heated at 125°C for 4 hours. Unfortunately, the water added was calculated based on the volume of the old vessels, which are approximately half the volume of the new vessels. Therefore the pressure in this reaction was only 50atm instead of 100atm as in the previous reactions. Figure 6-6 shows an SEM image of frustules from this reaction. The shape preservation was quite good. The fine features of the frustules are still visible. X–ray diffraction was done on this sample and the pattern is shown in Figure 6-7. Barium titanate, Titania, barium hydroxide, and barium carbonate are each present in this sample. The fact that titania and barium hydroxide were still present shows that the reaction did not go to completion. The presence of barium carbide is not surprising as the sample was

exposed to air for diffraction analysis. The incomplete reaction is not surprising since reaction temperature, time, and pressure were all lower in this sample than in the previously converted samples. Longer reaction time and higher pressure would likely bring the reaction to completion.

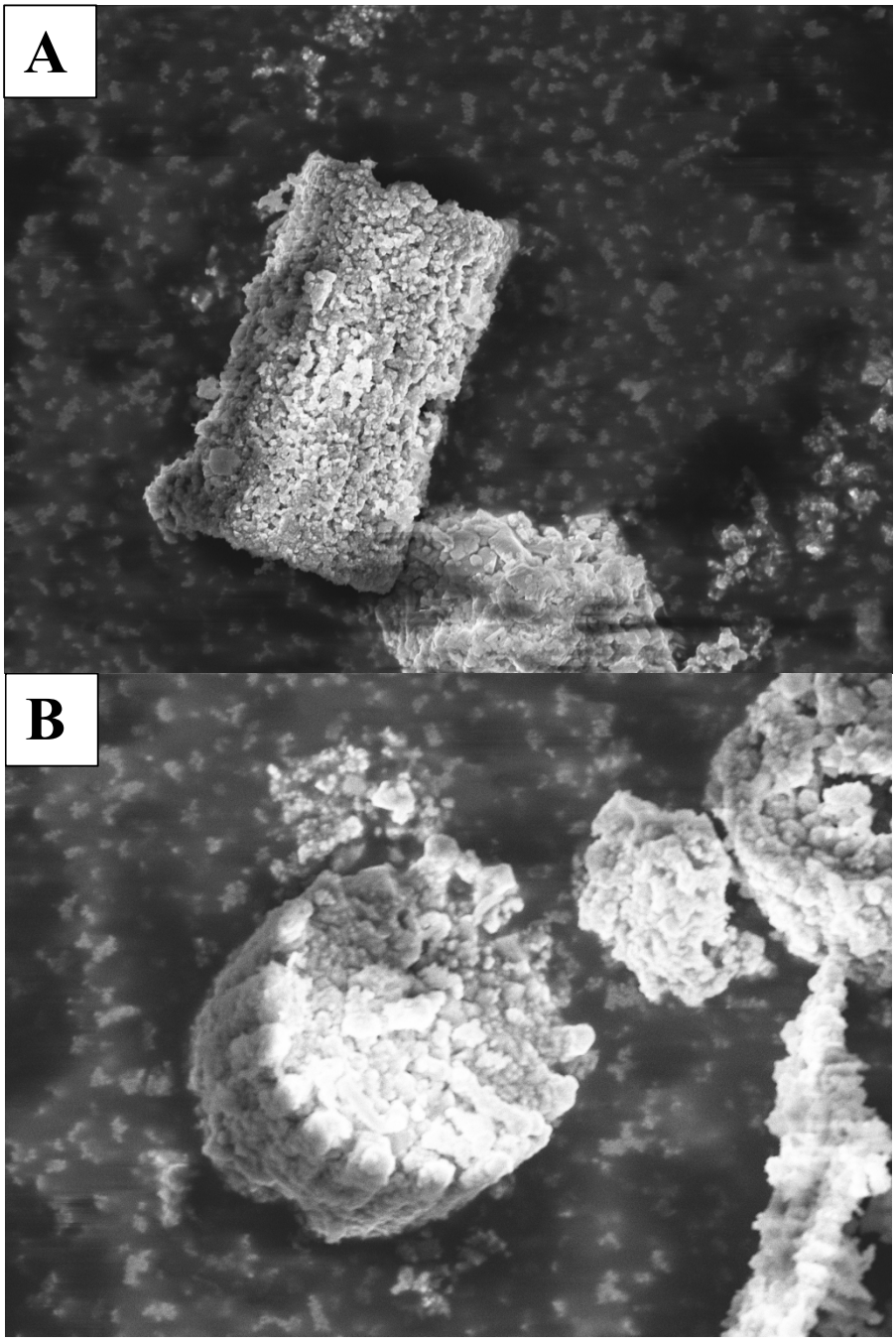

Figure 6-1 SEM images of samples reacted at 150°C

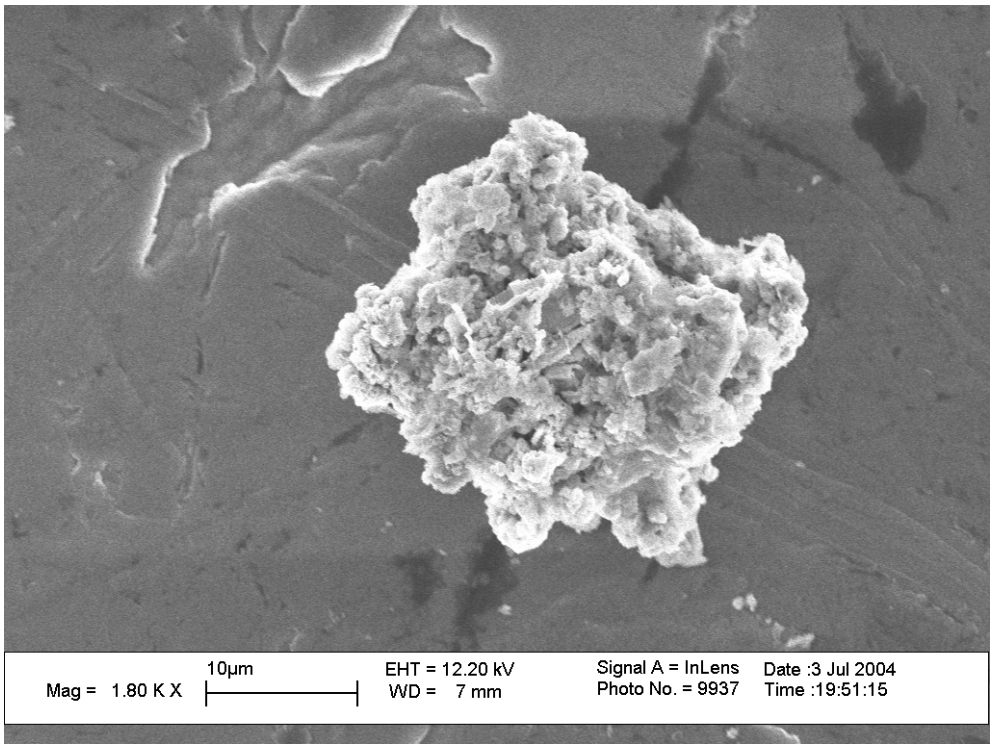

Figure 6-2 SEM image of the sample treated at 225°C

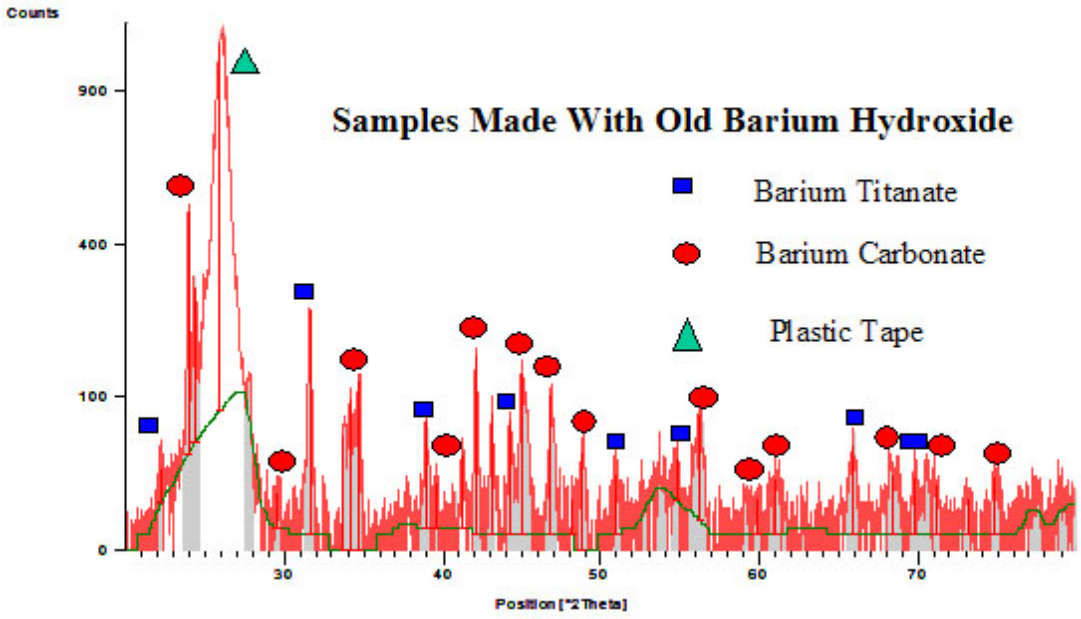

Figure 6-3 Representative X-ray diffraction pattern

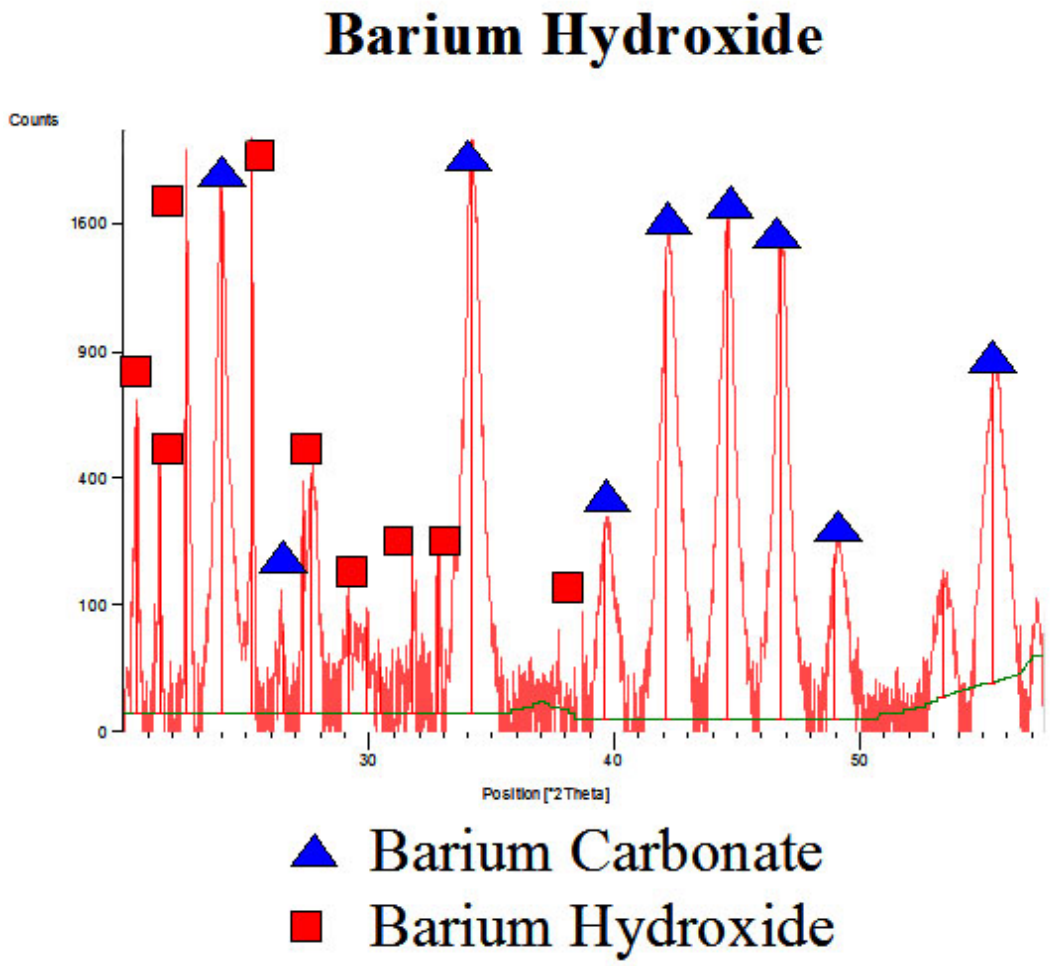

Figure 6-4 X-ray diffraction pattern of old Barium Hydroxide

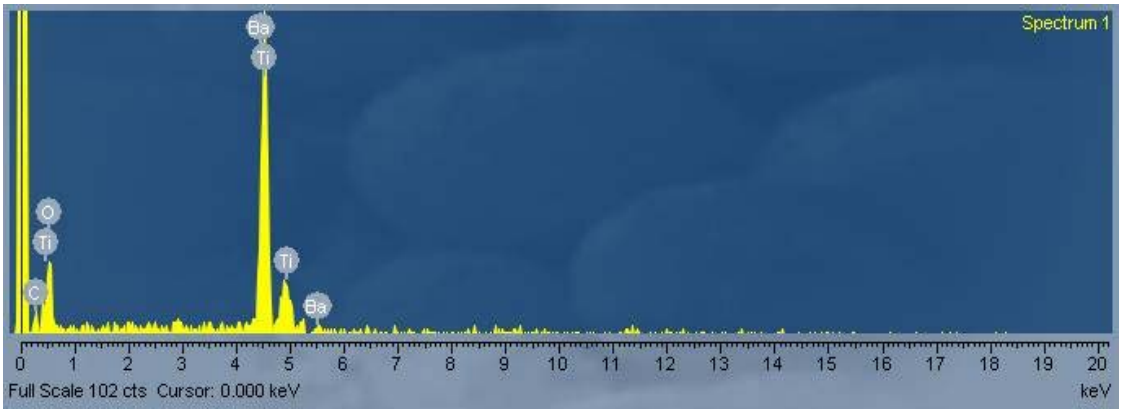

Figure 6-5 EDS spectrum showing the presence of Ti, Ba, O, and C

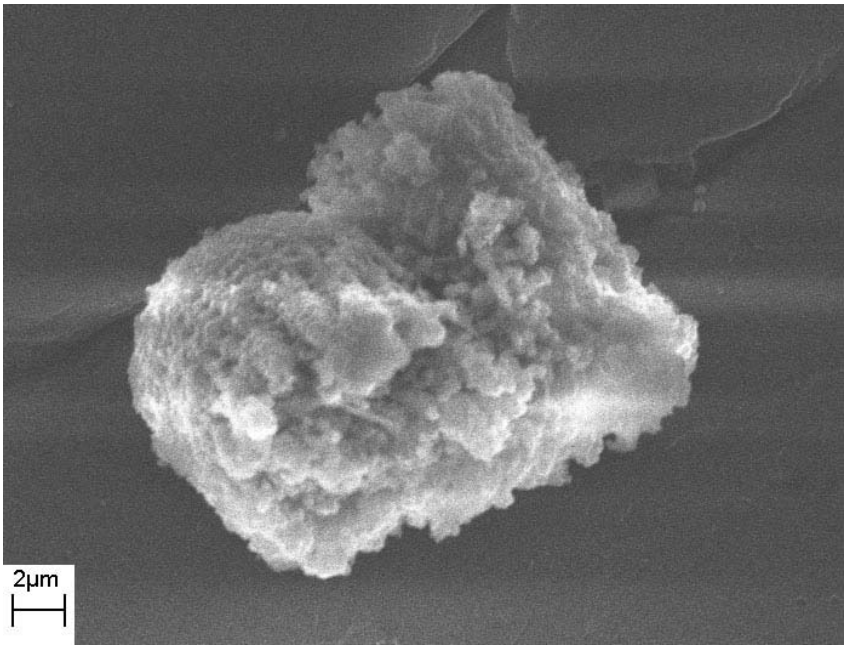

Figure 6-6 Image of sample prepared under argon heated to 125°C for 4h

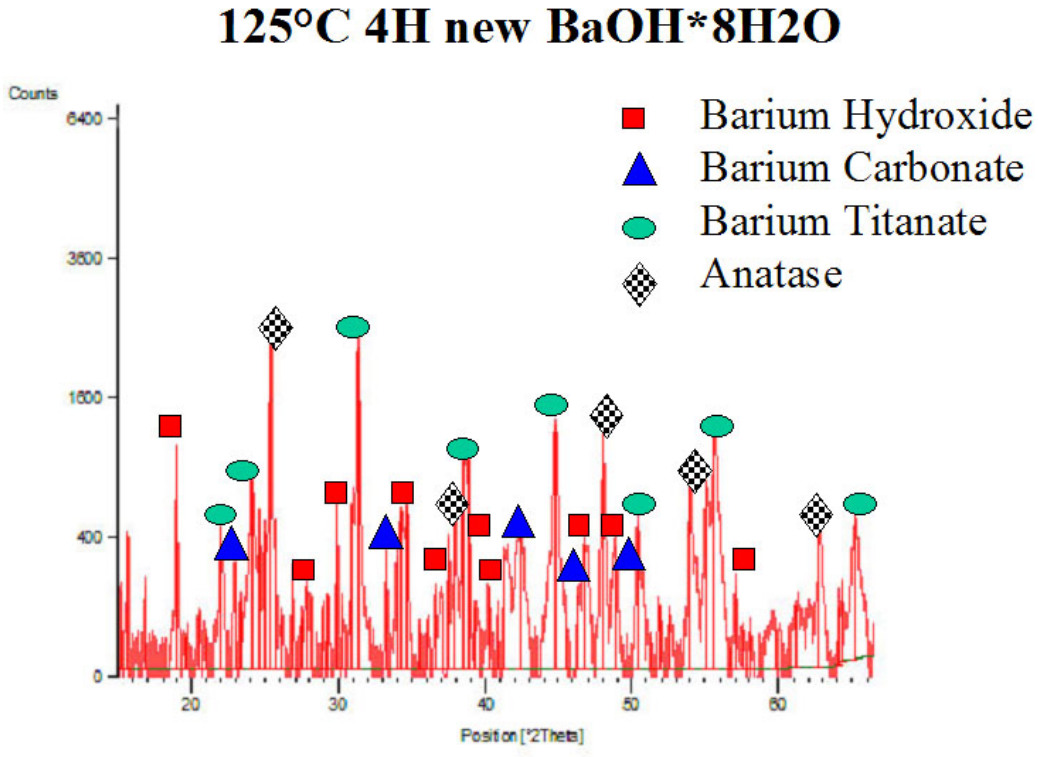

Figure 6-7 XRD pattern of sample prepared under argon heated to 125°C for 4h

References

(1) Sun, S., Anders, S., Thomson, T., Baglin, J. E. E., Toney, M. F., Hamann, H. F., Murray, C. B., Terris, B. D. Controlled synthesis and assembly of Fe-Pt nanoparticles. J. Phys. Chem. B 107, 5419-5425 (2003).

(2) Willner, I., Willner, B. Functional nanoparticle architectures for sensoric, optoelectronic, and bioelectronic applications. Pure Appl. Chem. 74, 1773-1783 (2002).

(3) Bimberg, D., Grundmann, M., Ledentsov, N. N., Mao, M. H., Ribbat, Ch., Sellin, R., Ustinov, V. M., Zhukov, A. E., Alferov, Zh. I., Lott, J. A. Novel infrared quantum dot lasers: theory and reality. Physica Status Solidi B 224, 787-796 (2001).

(4) Alivisatos, A. P. Semiconductor clusters, nanocrystals, and quantum dots. Science 271, 933-937 (1996).

(5) Crabb, C., Parkinson, G. The nanosphere: a brave new world. Chem. Eng. 109, 27-31 (2002).

(6) Whitesides, G. M., Mathias, J. P., Seto, C. T., Molecular self-assembly and nanochemistry: a chemical strategy for the synthesis of nanostructures. Science 254, 1312-1319 (1991).

(7) Niemeyer, C. M. Nanoparticles, proteins, and nucleic acids: biotechnology meets materials science. Angew. Chem. Int. Ed. 40, 4128-4158 (2001).

(8) Lowenstam, H. A. Minerals formed by organisms. Science 211, 1126-1131 (1981).

(9) Schuler, D., Frankel, R. B. Bacterial magnetosomes: microbiology, biomineralization and biotechnological applications. Appl. Microbiol. Biotechnol. 52, 464-473 (1999).

(10) Crawford, S. A., Higgins, M. J., Mulvaney, P., Wetherbee, R. Nanostructure of the diatom frustule as revealed by atomic force and scanning electron microscopy. J. Phycol. 37, 543-554 (2001).

(11) Round, F. E., Crawford, R. M., Mann, D. G. The Diatoms: Biology and Morphology of the Genera (Cambridge University Press, Cambridge, 1990).

(12) Werner, D. The Biology of Diatoms (Univ. California Press, Berkeley, CA, 1977).

(13) Veronique, M.-J., Hildebrand, M., Brzezinski, M. A. Silicon metabolism in diatoms: implications for growth. J. Phycol. 36, 821-840 (2000).

(14) Lebeau, T., Robert, J.-M. Diatom cultivation and biotechnologically relevant products. Part I: cultivation at various scales. Appl. Microbiol. Biotechnol. 60, 612-623 (2003).

(15) Parkinson, J., Gordon, R. Beyond micromachining: the potential of diatoms. Trends Biotechnol. 17, 190-196 (1999).

(16) Mehard, C. W., Sullivan, C. W., Azam, F., Volcani, B. E., Role of silicon in diatom metabolism. IV. Subcellular localization of silicon and germanium in Nitzschia alba and Cylindrotheca fusiformis. Physiol. Plant. 30, 265-272 (1974).

(17) Sandhage, K. H., Dickerson, M. B., Husman, P. M., Caranna, M. A., Clifton, J. D., Bull, T. A., Heibel, T. J., Overton, W. R., Schoenwaelder, M. E. A. Novel, bioclastic route to self-assembled, 3-D, chemically-tailored meso/nanostructures: shape- preserving reactive conversion of biosilica (diatom) microshells. Adv. Mater. 14, 429-433 (2002).

(18) Sandhage, K. H., Dickerson, M. B., Huseman, P. M., Zalar, F. M., Rondon, M. R., Sandhage, E. C. A Novel Hybrid Route to Chemically-Tailored, Three-Dimensional Oxide Nanostructures: The BaSIC (Bioclastic and Shape-Preserving Inorganic Conversion) Process. Ceram. Eng. Sci. Proc. 23, 653-664 (200)

(19) Caracoche, M. C., Rivas, P. C., Cervera, M. M., Caruso, R., Benavidez, E., de Sanctis, O., Escobar, M. E. Zirconium oxide structure prepared by the sol-gel route: I, the role of the alcoholic solvent. J. Am. Ceram. Soc. 83, 377-384 (2000).

(20) Stefanic, I. I., Music, S., Stefanic. G., Gajovic, A., Thermal behavior of ZrO_2 precursors obtained by sol-gel processing, J. Mol. Struct. 480-481, 621-625 (1999).

(21) Stachs, O., Gerber, Th., Petkov, V. The structure formation of zirconium oxide gels in alcoholic solution. J. Sol-Gel Sci. Techn., 15, 23-30 (1999).

(22) B. D. Cullity, Elements of X-ray Diffraction 101-102 (Addison-Wesley Publishing Co., Reading, MA, 1978).

(23) Tichit, D.; Coq, B.; Armendariz, H.; Figueras, F. One-step sol-gel synthesis of sulfated-zirconia catalysts. Catalysis Letters 38, 109-13 (1996).

(24) Shevchenko, A. V., Dudnik, E. V., Ruban, A. K., Red'ko, V. P., Vereschaka, V. M., Lopato, L. M. Nanocrystalline Powders Based on ZrO_2 for Biomedical Applications and Power Engineering. Powder Metall. Metal Ceram. 41, 558-563 (2002).

(25) Burkhard, D. J. M., Hanson, B., Ulmer, G. C., ZrO_2 oxygen sensors: an evaluation of behavior at temperatures as low as 300°C. Solid State Ionics 47, 169-175 (1991).

(26) Swain, M. V. Transformation toughened non-oxide zirconia composite ceramics. Materials Forum 11, 202-9 (1988).

(27) Dunahay, T. G., Jarvis, E. E., Roessler, P. G. Genetic transformation of the diatoms Cyclotella Cryptica and Navicula Saprophila. J. Phycol. 31, 1004-1012 (1995).

(28) Zaslavskaia, L. A., Lippmeier, J. C., Kroth, P. G., Grossman, A. R., Apt, K. E., Transformation of the diatom Phaeodactylum Tricornutum (bacillariophyceae) with a variety of selectable marker and reporter genes. J. Phycol. 36, 379-386 (2000).

(29) Web sites: http://genome.jgi-psf.org/thaps0/thaps0.info.html
http://www.jgi.doe.gov/genomes/index.html

(30) Yang, Y.; Zeng, C.; Lee, L. J. *Adv. Mater.* 2004, *16*, 560.

(31) Armani, D.; Liu, C. *J. Micromech. Microeng.* 2000, *10*, 80.

(33) Lee, L. P.; Berger, S. A.; Liepmann, D.; Pruitt, L. *Sensors and Actuators* 1998, *A71*, 144.

(32) Kroeger, Silke; Turner, Anthony P. F.; Mosbach, Klaus; Haupt, Karsten. Imprinted Polymer-Based Sensor System for Herbicides Using Differential-Pulse Voltammetry on Screen-Printed Electrodes. Analytical Chemistry (1999), 71(17), 3698-3702.

(34) Embleton, J. K.; Tighe, B. J. *J. Microencaps.* 1992, *9*, 73.

(35) Seiller, M.; Martini, M.-C.; Benita, S. in *Microencapsulation: Methods and Industrial Applications*; Marcel Dekker: New York, NY, 1996, p. 588.

(36) Xu, T.-B.; Su, J.; Zhang, Q. *SPIE Proc.* 2003, *5055*, 66.

(37) Markus, A. in *Microencapsulation: Methods and Industrial Applications*; Marcel Dekker: New York, NY, 1996, p. 73.

(38) Heo, J.-S.; Park, N.-H.; Ryu, J.-H.; Choi, G.-H.; Suh, K.-D. *Macromol. Chem. Phys.* 2003, *204*, 2002.

(39) Joshi, M. P.; Pudavar, H. E.; Swiatkiewicz, J.; Prasad, P. N.; Reianhardt, B. A. *Appl. Phys. Lett.* 1999, *74*, 170.

(40) Parthenopoulos, D. A.; Rentzepis, P. M. *Science* 1989, *245*, 843.

(41) Ahn, C. H. *Polymer Preprints* 2003, 44, 530.

(42) Ballandras, S.; Calin, M.; Zissi, S.; Bertsch, A.; Andre, J. C.; Hauden, D. *Sensors and Actuators* 1997, *A62*, 741.

(43) Varadan, V. K.; Varadan, V. V. *SPIE Proc.* 1999, 3879, 116.

(44) Rotting, O.; Ropke, W.; Becker, H.; Gartner, C. in *Microsystem Technologies 8*; Springer-Verlag: 2002, p. 32.

(45) Bauerlein, E. *Angew. Chem. Int. Ed.* 2003, *42*, 614.

(46) Weaver, J. C.; Pietrasanta, L. I.; Hedin, N.; Chmelka, B. F.; Hansma, P. K.; Morse, D. E. *J. Struct. Biol.* 2003, *144*, 271.

(47) Mann, S. *Nature* 1993, *365*, 499.

(48) Tappan, H. *The Paleobiology of Plant Protists*; W. H. Freeman & Company: San Francisco, CA, 1980.

(49) Round, F. E.; Crawford, R. M.; Mann, D. G. *The Diatoms: Biology & Morphology of the Genera*; Cambridge University Press: Cambridge, England, 1990.

(50) Werner, D. in *The Biology of Diatoms*; Blackwell Scientific Publications: Oxford, England, 1977, p. 1.

(51) Noll, F.; Sumper, M.; Hampp, N. *Nano Lett.* 2002, *2*, 91.

(52) Crawford, S. A.; Higgins, M. J.; Mulvaney, P.; Wetherbee, R. *J. Phycol.* 2001, *37*, 543.

(53) Hildebrand, M; Wetherbee, R. *Progress in Molecular and Subcellular Biology*, Vol. 33; Springer-Verlag: Berlin, Germany, 2003, p. 11.

(54) Mann, D. G.; Droop, S. J. M. *Hydrobiologia* 1996, *336*, 19.

(55) Martin-Jezequel, V.; Hildebrand, M.; Brzezinski, M. A. *J. Phycol.* 2000, *36*, 821.

(56) Weber, J. N.; White, E. W. *Science* 1972, *176*, 922.

(57) Skinner, D. P.; Newnham, R. E.; Cross, L. E. *Mater. Res. Bull.* 1978, *13*, 599.

(58) Lowenstam, H. A.; Weiner, S. in *Biomineralization and Biological Metal Accumulation*; D. Reidel Publishing Co.: Hingham, MA, 1983, p.191.

(59) Website of the Joint Genome Institute: http://genome.jgi-psf.org/diatom/index.html

(60) Lebeau, T.; Robert, J.-M. *Appl. Microbiol. Biotechnol*. 2003, *60*, 612.